# Field Ionization and Field Emission
# with Intense, Single-cycle THz Pulses
# Need to replace with my own title

by

© Yunxiao Wang

A thesis submitted to the

School of Graduate Studies

in partial fulfilment of the

requirements for the degree of

Anqing, Anhui, China

B.S. in Physics University of Science and Technology of China May 2009

Memorial University of Newfoundland

Doctor of Philosophy

St. John's                                            Newfoundland

Department of Physics August, 2016

# Abstract

Nuclear-polarized $^3$He targets have been widely used in electron-scattering experiments in Thomas Jefferson National Accelerator Facility (JLAB) since mid 1990s. It is of great importance to produce large amounts of $^3$He gas with high polarization.

The latest experiments run in JLAB prior to the 12GeV upgrade have been using cells polarized with Spin-Exchange Optical Pumping (SEOP). These cells were made of the GE180 glass and use a two-chambered design. The top chamber, known as the pumping chamber, is where $^3$He is polarized through SEOP. The bottom chamber, known as the target chamber, is where electron scattering occurs. Great effort has been made in our lab to develop this generation of cells. Alkali-hybrid SEOP together with narrowband laser diode arrays have increased the $^3$He polarization from 37% to 65%. Among other things, we also carefully studied an additional spin relaxation mechanism that limits the maximum achievable $^3$He polarization.

The 12GeV upgrade makes the future experiments much more demanding in terms of target cell performance. One challenge it brings is the high relaxation due to electron beam. We have designed and tested a new style cell that uses convection instead of diffusion to increase the rate at which the polarization in the target chamber is being replenished by gas from pumping chamber. We have obtained over 50% polarization with controllable convection speed so far.

An additional problem that comes with higher beam current is that the glass end windows of traditional design are not likely to survive the experiments. Our group started exploring the option of using metal end windows from a decade ago. The first problem to solve is to find out the correct material and the proper technique

to incorporate metal without introducing significant spin relaxation and still being able to hold high pressure gas (12 atm) inside. This is a brand new technique that may have a profound impact of future cell designs once fully developed. Although no metal end windows have been tested so far, multiple glass cells with different kinds metal tubes (much larger in area compared to the end windows that will be used in JLAB experiments) attached were examined and were enough to convince us the extra spin relaxation is not likely to cause significant problems. The metals tubes were connected to Pyrex glass with knife-edge (housekeeper) seals and stayed intact through high pressure tests. After exploring options such as pure copper, gold coated copper, titanium, stainless steel, gold coated titanium, we have established that electroplating gold on copper substrate yields the best result so far. Further tests are planned before attaching metal end windows to GE180 glass and using them in electron-scattering experiments.

# Acknowledgements

Put your acknowledgements here...

*"Intellectual and practical assistance, advice, encouragement and sources of monetary support should be acknowledged. It is appropriate to acknowledge the prior publication of any material included in the thesis either in this section or in the introductory chapter of the thesis."*

<div align="right">

— MUN School of Graduate Studies

</div>

# Contents

# List of Tables

# List of Figures

# Chapter 1

# Spin-Exchange Optical Pumping

## 1.1   Overview

Spin-polarized noble gases have been widely used for various purposes. In JLAB, polarized $^3$He is used as target for electron-scattering experiments. This is because a $^3$He nucleus has a pair of protons with paired spins and a single neutron that contributes the most of the nuclear spin. In MRI, polarized $^3$He has seen uses such as detecting structural damage in the lungs.

There are generally two ways of polarizing $^3$He: Metastability-Exchange Optical Pumping (MEOP) and Spin-Exchange Optical Pumping (SEOP). Our group focuses on SEOP as MEOP polarizes gas at relatively low pressure ($\sim$1 torr), thus further compression is required to produce target cells of several atms that meet the need of JLab experiments.

In SEOP, alkali metal is polarized by circularly polarized laser tuned to the D1 transition of the particular alkali species used. $^3$He obtains polarization from alkali

metal through spin exchange process. With the combination of hybrid alkali mixtures (typically Rb and K) and spectrally narrowed lasers, more than 70% polarizations have been produced.

## 1.2   Optical pumping

### 1.2.1   Rb for SEOP

In optical pumping, Rb is often the alkali metal chosen to be optically pumped by circularly polarized laser light. The angular momentum of a polarized photon is transfered to the valence electron of Rb atom. In the case of hybrid mixture of Rb/K, Rb is still the alkali metal that is directly pumped by laser light while K serves as an efficient medium to transfer the polarization from Rb to $^{3}$He. Because the spin destruction rates are much lower for lighter alkali metals, K-$^{3}$He spin-exchange process is a lot more efficient than that of Rb-$^{3}$He. However, it is still much easier to optically pump Rb and transfer the polarization to $^{3}$He through K, mainly for Rb's low melting point, the relative ease of acquiring laser at the Rb D1 line wavelength and the wide separation between D1 (794.7nm) and D2 line (780nm).

The Rb melting point is at 39.5°C, so it's easy to achieve enough Rb vapor without having to drive the oven temperature too high. In our lab, depending on if the cell contains pure Rb or Rb/K mixture, the oven temperature can be between 85°C to as high as 255°C. Perhaps the most used oven temperature for hybrid is 235°C which has empirically been a good temperature to produce Rb/K mixture vapor, while 85°C is enough for pure Rb.

## 1.2.2 Vapor Pressure Curves

When the alkali metal is heated to above its melting point, a small amount of alkali metal atoms evaporate. The equilibrium vapor pressure is temperature dependent:

$$P = 10^{5.006+\alpha+\beta/T} Pa \tag{1.1}$$

where $\alpha$ and $\beta$ are listed in Table 1.2.2.

|  | Patassium | Rubidim |
|---|---|---|
| $\alpha$ | 4.402 | 4.312 |
| $\beta$ | -4453 | -4040 |

Thus the number density is

$$[A] = \frac{10^{5.006+\alpha+\beta/T}}{k_B T} \tag{1.2}$$

The number density curves of pure Rb and K vapor are shown in Fig. 1.1.

## 1.2.3 Energy Levels of Alkali Metal in External Magnetic Field

The Hamiltonian for ground state (L=0) alkali metal atoms in external magnetic field is:

$$\mathbf{H} = A\mathbf{I} \cdot \mathbf{S} + g_e \mu_B S_z B_z + g_N \mu_N I_z B_z \tag{1.3}$$

The first term $A\mathbf{I} \cdot \mathbf{S}$ describes the coupling of the nuclear spin $\mathbf{I}$ with the electron spin $\mathbf{S}$ and is key to spin exchange, where A is the isotropic magnetic-dipole coupling
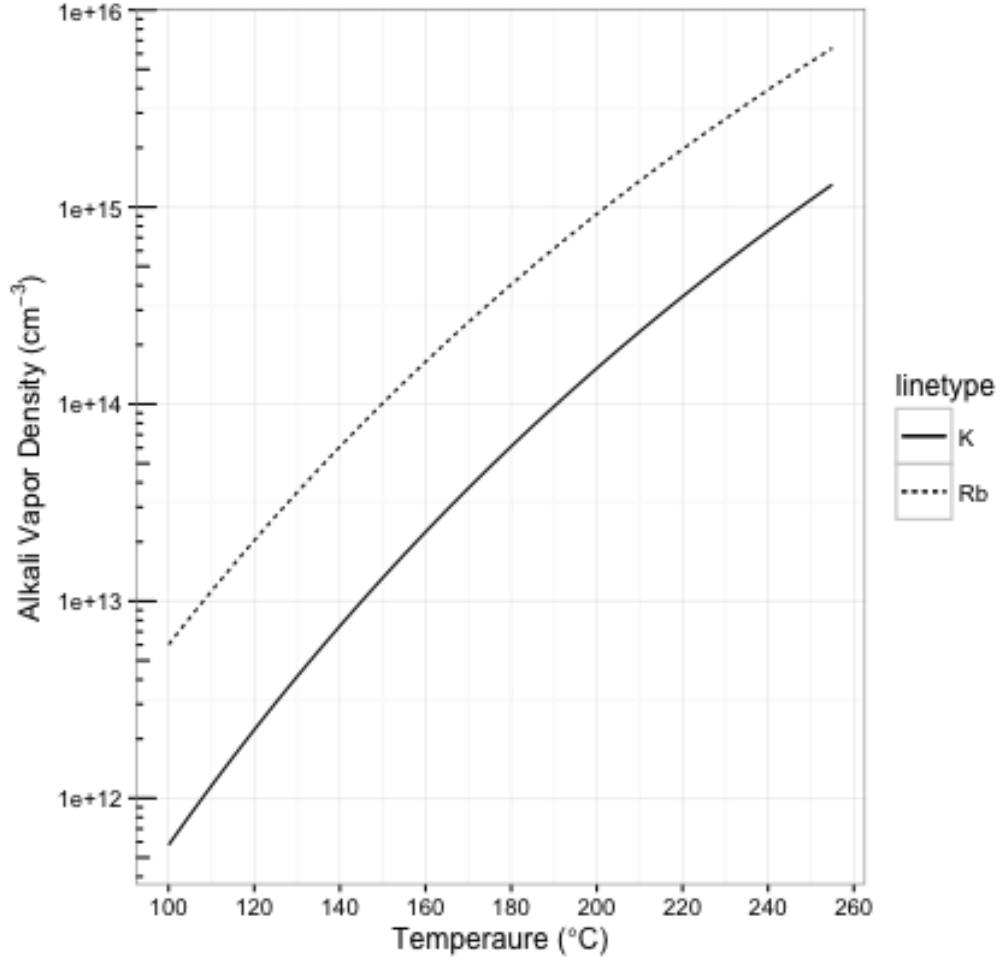
**Figure 1.1: Rb And K Number Density Curves**

coefficient. The resulting energy levels from the first term are referred to as hyperfine structure. The second and third terms describe the Zeeman splitting due to the presence of a weak external magnetic field. $\mu_B = 9.274 \times 10^{-24} J/T$ and $\mu_N = 5.051 \times 10^{-27} J/T$ are the Bohr and nuclear magnetons. $g_e \approx 2$ and $g_N \approx 5.59$ are the electronic and nuclear Lande g-factors.

The linear relationship between energy levels and magnetic field only holds for weak magnetic fields which applies to our lab where $\sim$13 Gauss is used most of the

4

time. When the Zeeman splitting grows comparable to the hyperfine energy difference one would have to take into account the quantum mixing of the states, the result is described by Breit-Rabi Formula. With ~13 Gauss, the hyperfine term dominates the total Hamiltonian. The energy levels of $^{87}$Rb are shown in Fig. 1.2.

## 1.2.4   Optical Pumping Process Overview

For simplicity, the following discussion will ignore the nuclear spins for now. The inclusion of nuclear spins will increase the number of energy states but the optical pumping mechanism remains the same. In our typical setup, circularly polarized laser light is tuned to the D1 line of Rb and excites valence electrons of Rb from $5S_{1/2}$ state to $5P_{1/2}$ state as shown in Fig. 1.3 ($2S_{1/2}$ and $2P_{1/2}$ states are used in the simple model described by the figure below).

Left-circularly polarized light is assumed in the figure, but either circular polarization works the same. Conservation of angular momentum requires $\Delta m = +1$ as the figure shows. Through collisions with other Rb atoms, excited electrons will mix and evenly distribute on the two $2P_{1/2}$ states. Electrons then decay to the two ground states with equal probabilities. The selection rule for the decay process is $\Delta m = 0$ or $\pm 1$. Even though both ground states receive electrons from the decay, only the m = -1/2 state absorbs the circular polarized photons and is being depleted, so atoms are in effect pumped to the m = +1/2 state. When we consider Rb with nuclear spins, both $5S_{1/2}$ and $5P_{1/2}$ states are split into more energy levels, but the net effect is still that the ground state with highest m accumulate atoms over time.

When the excited electrons decay back to the ground state, they emit unpolarized
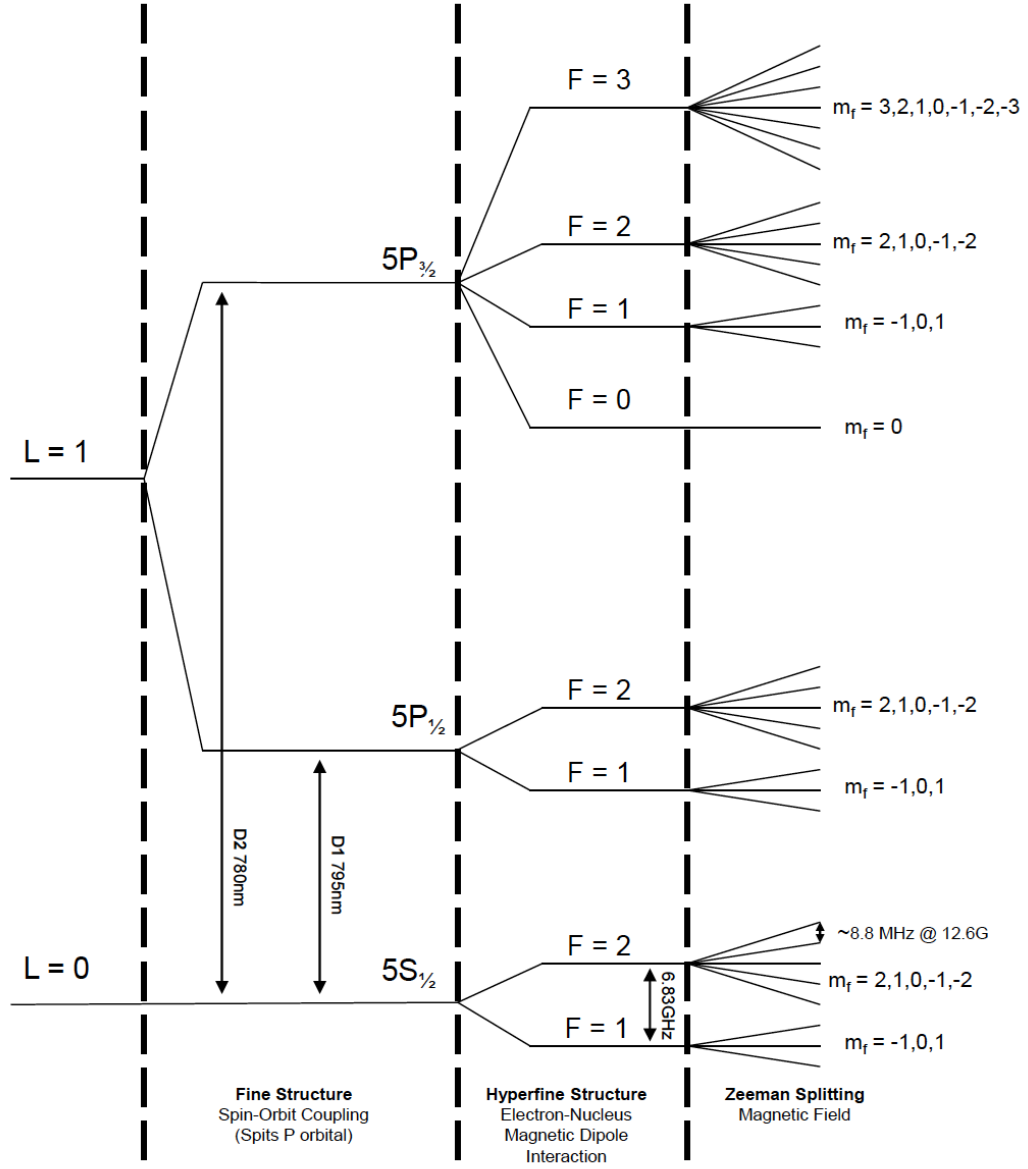
**Figure 1.2:** Level Diagram of $^{87}$Rb. The splittings are not to scale. Adapted from Dolph's PhD thesis.

photons with angular momentum in random directions which can depolarize the gas. A small amount of $N_2$ gas is added into the cell (typically around 0.1 Amagats) to non-radiatively quench the excited electrons as $N_2$ molecules can absorb the released
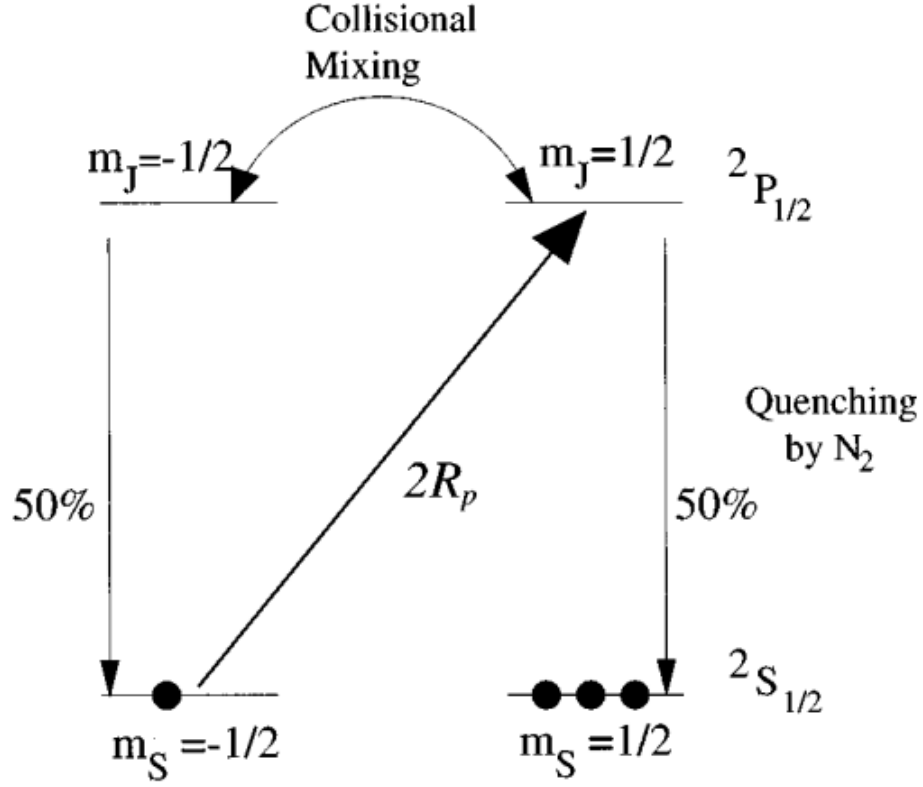
**Figure 1.3: The interaction of alkali-metal atoms with left-circularly ($\sigma^+$) polarized light. (from Ref. [?])**

energy of spontaneous decays into their rotational and vibrational modes of oscillation. With an appropriate amount of $N_2$, the photon-emitting decays can be reduced to less than 5%.

## 1.2.5   Optical Pumping Rate

The optical pumping rate at position $\vec{r}$ can be described by

**Table 1.1:** Pressure broadening of Rb $D_1$ lines by $^3$He, $^4$He and $N_2$. The broadening and shifting density coefficients are listed. The 4th and 6th columns are the temperature dependence for He and $N_2$, respectively. All coefficients are given for 353 K, values for different temperatures can be calculated with the temperature dependence.

|  | $^4$He | $^3$He | Temp. depen. | $N_2$ | Temp. depen. |
|---|---|---|---|---|---|
| $D_1$ full width (GHz/amg) | 18.0±0.2 | 18.7±0.3 | $T^{0.05\pm0.05}$ | 17.8±0.3 | $T^{0.3}$ |
| $D_1$ line shift (GHz/amg) | 4.3±0.1 | 5.64±0.15 | $T^{1.1\pm0.1}$ | -8.25±0.15 | $T^{0.3}$ |

$$R = \int \Phi(\nu, \vec{r})\sigma(\nu)d\nu \tag{1.4}$$

where $\Phi(\nu, \vec{r})$ is the position dependent photon spectral flux density and $\sigma(\nu)$ is the photon absorption cross section. The cross section has a natural Lorentzian lineshape which is broadened by Doppler effect and pressure broadening. The pressure broadening effect dominates the lineshape as our cells normally have densities well above one amagat. The collisions of Rb with $^3$He and $N_2$ cause the broadening as well as a slight shift of the $D_1$ line. The coefficients of pressure broadening for $^3$He, $^4$He and $N_2$ are listed in Table 1.1, and can be used to calculate the broadened line width and the shifted line center.

$\sigma(\nu)$ follows the sum rule:
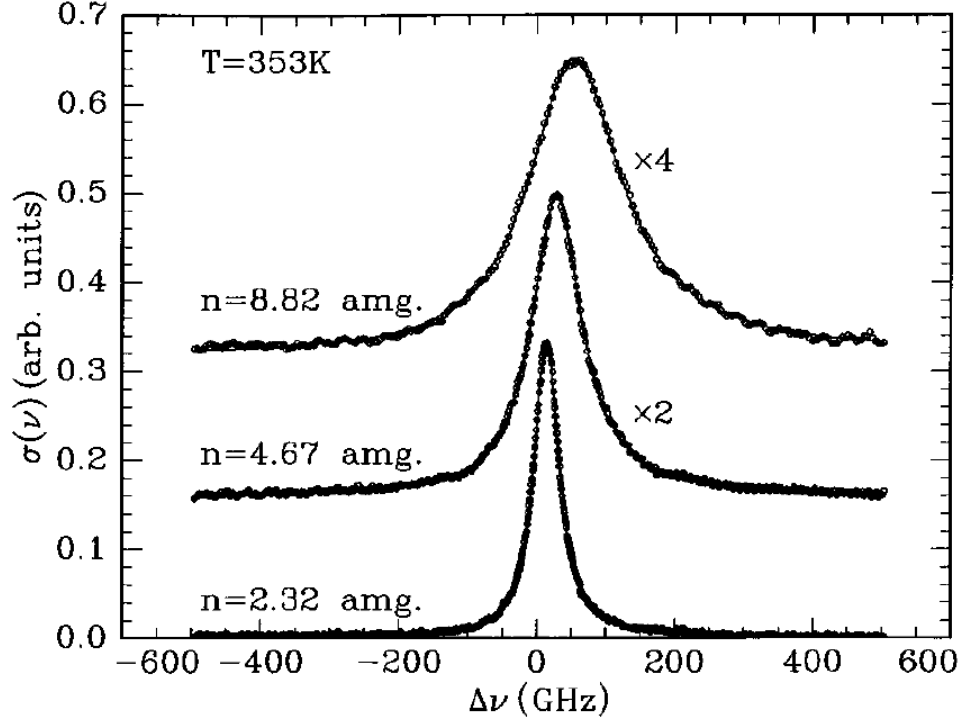
**Figure 1.4: Absorption cross section for Rb $D_1$ line in the presence of three different densities of $^3$He. (from Ref. [?])**

$$\int \sigma(\nu)d\nu = \pi r_0 c f \qquad (1.5)$$

where $r_0 = 2.82 \times 10^{-13}$ cm is the classical electron radius and f=0.337is the transition oscillator strength. Thus the photon absorption cross section can be described by Lorentzian lineshape:

$$\sigma(\nu) = f r_e c \frac{\frac{\Gamma_A}{2}}{(\nu - \nu_0)^2 + (\frac{\Gamma_A}{2})^2} \qquad (1.6)$$

where $\Gamma_A$ is the pressure dependent FWHM, $\Gamma_A \approx 0.04 nm/amg \cdot [^3He]$. At the front of the cell, the photon spectral flux density is the product of a Gaussian spatial
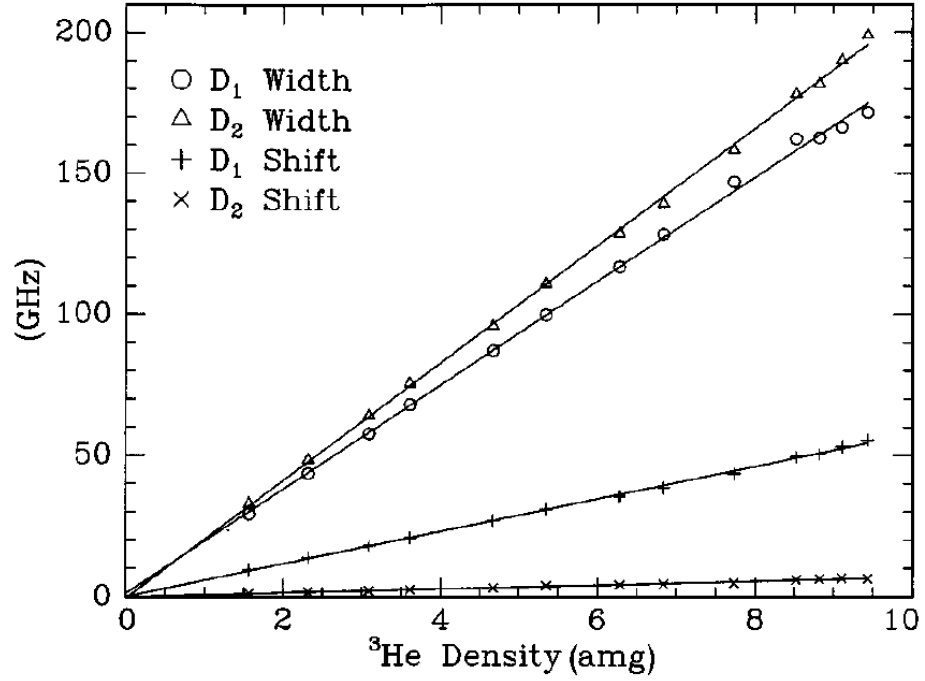
**Figure 1.5: The shift and the broadening due to presence of $^3$He for Rb $D_1$ and $D_2$ lines. (from Ref. [?])**

distribution and a Gaussian spectrum.

$$\phi(\nu, \vec{r}) = \phi_0(\vec{r})G(\nu) \tag{1.7a}$$

$$\phi_0(\vec{r}) = \frac{P}{h\nu}\frac{2}{\omega^2\pi}e^{2r^2/\omega^2} \tag{1.7b}$$

$$G(\nu) = \frac{1}{\sqrt{2\pi}\sigma_l}e^{-(\nu-\nu_l)^2/2\sigma_l^2} \tag{1.7c}$$

where P is the laser power; $\omega$ is the beam waist; $\sigma_l$ is the Gaussian width of the laser and $\nu_l$ is the central laser frequency.

## 1.2.6 Polarization Time Evolution

Polarizations of Rb electrons are more complex, but $^3He$ nuclei have an intrinsic nuclear spin of 1/2, and it is simpler to explain the math with spin of 1/2. Let's define the polarization as the asymetry between +1/2 state and -1/2 state:

$$P = \frac{\rho_{+1/2} - \rho_{-1/2}}{\rho_{+1/2} + \rho_{-1/2}} = \rho_{+1/2} - \rho_{-1/2} \qquad (1.8)$$

where $\rho_{\pm1/2}$ is the population in the $\pm1/2$ state.

The time evolution of polarization for both Rb electrons and $^3He$ follows the equation:

$$\frac{dP}{dt} = \gamma(1 - P) - \Gamma \cdot P \qquad (1.9)$$

$\gamma$ is the polarization rate and $\Gamma$ is the depolarization rate in the above differential equation. The solution has the simple form of:

$$P(t) = Ce^{-(\gamma+\Gamma)t} + \frac{\gamma}{\gamma + \Gamma} \qquad (1.10)$$

Note the depolarization rate also contributes to the rate at which P approaches saturation as it lowers the saturated polarization hence shortens the time to reach it. The saturated polarization is defined as the value of P in the limit t → ∞:

$$P_\infty = \frac{\gamma}{\gamma + \Gamma} \qquad (1.11)$$

The initial polarization is defined as the value of P at t = 0:

$$P_0 = C + \frac{\gamma}{\gamma + \Gamma} = C + P_\infty \qquad (1.12)$$

11

Thus, P(t) can be expressed as:

$$P(t) = (P_0 - P_\infty)e^{-(\gamma+\Gamma)t} + P_\infty \tag{1.13}$$

In the case of polarizing Rb with a pump laser, $\gamma$ is the pumping rate R and $\Gamma$ is the Rb spin relaxation rate $\Gamma_{Rb}$. There is typically a small angle $\theta$ between the pump laser and the holding field even though great effort has been made to minimize the angle. Thus P(t) can be rewritten as:

$$P(t) = P_0 e^{-(R+\Gamma_{Rb})t} + P_{laser}cos\theta\frac{R}{R+\Gamma_{Rb}}(1 - e^{-(R+\Gamma_{Rb})t}) \tag{1.14}$$

$\theta$ is called the skew angle, $P_{laser}$ is the circular polarization of the pump laser which is above 99.5%. Rb close to the front side of the cell can reach above 97% (depends on the laser power and other factors) on the order of 100's of microseconds. As the laser propagates through the cell, power is attenuated by Rb vapor. Therefore Rb polarization at the back side of the cell is lower than that at the front side. One way to overcome the problem is to shine pump laser from both sides of the cell which would lead to higher overall Rb polarization and $^3$He polarization.

Spins are thermally polarized with the presence of a magnetic field even without external pumping source. The probability for a spin to be in state s is:

$$Prob. = \frac{e^{-E_s/k_BT}}{\sum_{si} e^{-E_{si}/k_BT}} \tag{1.15}$$

where $E_s$ is the energy of the state, $k_B$ is the Boltzmann constant and T is the temperature. Using the thermal distribution, under typical operating conditions, $^3He$ polarization is $10^{-9}$ and Rb polarization is $10^{-5}$. Both are negligible without active

pumping.

## 1.2.7  Rb Spin Destruction Rate

There are two main mechanisms of Rb depolarization: the binary collisions with Rb, $^3$He and $N_2$, and the formation and breakup of van der Waals molecules, the second mechanism is negligible for $^3$He cells. The Rb spin destruction rate can then be expressed as

$$\Gamma_{Rb} = k_{Rb-Rb}[Rb] + k_{Rb-^3He}[^3He] + k_{Rb-N_2}[N_2] \tag{1.16}$$

where $k_{Rb-X}$ is the spin destruction rate constant and $[X]$ is the density of X. Dolph has summarized these constants based on measurements from various groups:

$$k_{Rb-^3He}(T) = 55.9(9) \left(\frac{T}{473.15K}\right)^{3.31(12)} Hz/amg \tag{1.17a}$$

$$k_{Rb-N_2}(T) = 290(30) \left(\frac{T}{473.15K}\right)^{2.0(25)} Hz/amg \tag{1.17b}$$

$$k_{Rb-Rb} = 4.813(48) \times 10^{-13} Hz \cdot cm^3 \tag{1.17c}$$

For a pure Rb cell at 170°C with the following densities in the pumping chamber:

$$[^3He] \approx 8.0 amg \tag{1.18a}$$

$$[N_2] \approx 0.08 amg \tag{1.18b}$$

$$[Rb] \approx 6.0 \times 10^{14} cm^{-3} \tag{1.18c}$$

The approximate spin destruction rates due to various gases are:

13

$$\Gamma_{Rb-^3He} \approx 360 Hz \tag{1.19a}$$

$$\Gamma_{Rb-N_2} \approx 20 Hz \tag{1.19b}$$

$$\Gamma_{Rb-Rb} \approx 289 Hz \tag{1.19c}$$

The total spin destruction rate is 669 Hz. With more than 20 W narrowband laser, the optical pumping rate is often 100s kHz, which is much greater than the total Rb spin destruction rate. Therefore, it is very easy to achieve a close to unity alkali polarization.

## 1.3 Spin Exchange

Following equation 1.14, the time evolution of $^3He$ polarization can be expressed as:

$$P_{^3He}(t) = P_0 e^{-(\gamma_{se}+\Gamma)t} + P_{Rb}\frac{\gamma_{se}}{\gamma_{se}+\Gamma}(1 - e^{-(\gamma_{se}+\Gamma)t}) \tag{1.20}$$

The saturation polarization is

$$P_\infty = P_{Rb}\frac{\gamma_{se}}{\gamma_{se}+\Gamma} \tag{1.21}$$

where $\gamma_{se}$ is the spin exchange rate between $^3$He and Rb, and $\Gamma$ is the spin relaxation rate.

### 1.3.1 Spin-Dependent Interactions

The key process in spin-exchange optical pumping is collisional transfer of polarization between optically pumped alkali-metal atoms and the nuclei of the noble gas atoms.

As in Fig. 1.6, the transfer of angular momentum occurs either while the atoms are bound in van der Waals molecules or in simple binary collisions. For $^3He$, binary collisions dominate, and the contribution from van der Waals molecules is negligible. The time scale for binary collisions is on the order of $10^{-12}$ sec, the collision can induce both $\Delta F = \pm 1$ and $\Delta F = 0$ transitions between hyperfine sublevels. For heavier noble gases like $^{129}$Xe at pressure of a few tens of Torr, the contributions of van der Waals molecuels can greatly exceed that of binary collisions. At several atms which is the typical operating pressure for SEOP, the time scale of van der Waals molecules is greatly limited by collision so that the binary collisions dominate.

Spin-dependent interactions produce the spin transfer and relaxation. For SEOP, spin-rotation interaction between $\vec{S}$ and the rotational angular momentum $\vec{N}$ of the atom pair formed by Rb and noble gas atom, and the isotropic hyperfine interaction between $\vec{S}$ and the noble-gas nuclear spin $\vec{I}_b$ dominate the spin-exchange process:

$$V_1(\vec{R}) = \gamma(R)\vec{N} \cdot \vec{S} + A(R)\vec{I}_b \cdot \vec{S} \qquad (1.22)$$

The spin-rotation interaction is caused by the magnetic fields from relative motion of the charges of the colliding atoms, and the isotropic hyperfine interaction comes from the magnetic field inside the nucleus of the noble-gas atom. The spin-rotation interaction produces relaxation of the alkali-metal electron-spins, while the isotropic hyperfine interaction transfers angular momentum back and forth between the alkali-metal electron spins and the noble-gas nuclear spins.

An alkali-metal atom and a noble-gas atom interact via both a large spin-independent interaction $V_0(R)$ and a small spin-dependent interaction $V_1(R)$. At the high oper-
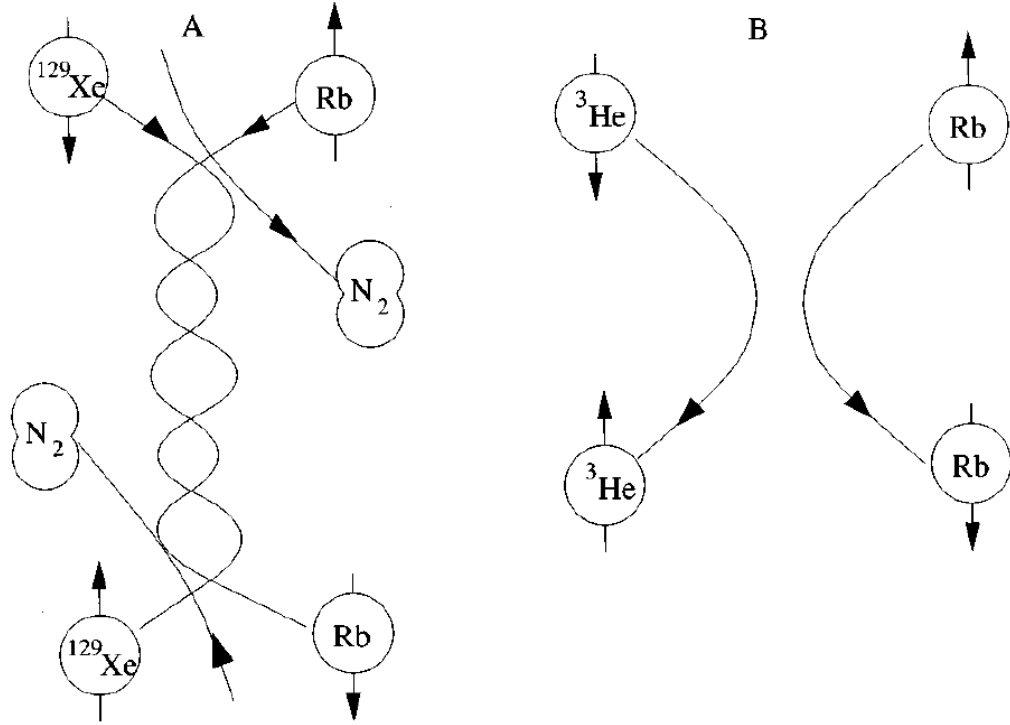
**Figure 1.6: A. Formation and breakup of alkali-metal/noble-gas van der Waals molecule. B. Binary collision between an alkali-metal atom and a noble-gas atom. (from Ref. [?])**

ating temperatures, $V_0$ determines classical collision trajectories, while $V_1$ acts as a small perturbation. We'll focus on $V_1$ below since it is responsible for spin exchange.

Including a few more terms that were neglected in Eq. 1.7, the spin-dependent interaction $V_1(R)$ can be expressed as:

$$V_1(\vec{R}) = \gamma(R)\vec{N} \cdot \vec{S} + \sum_k A_k(R)\vec{I}_k \cdot \vec{S}$$

$$+ \sum_k B_k(R)\vec{I}_k \cdot (3\vec{R}\vec{R} - 1) \cdot \vec{S} \qquad (1.23)$$

$$+ \sum_k C_k(R)\vec{I}_k \cdot (3\vec{R}\vec{R} - 1) \cdot \vec{I}_k$$
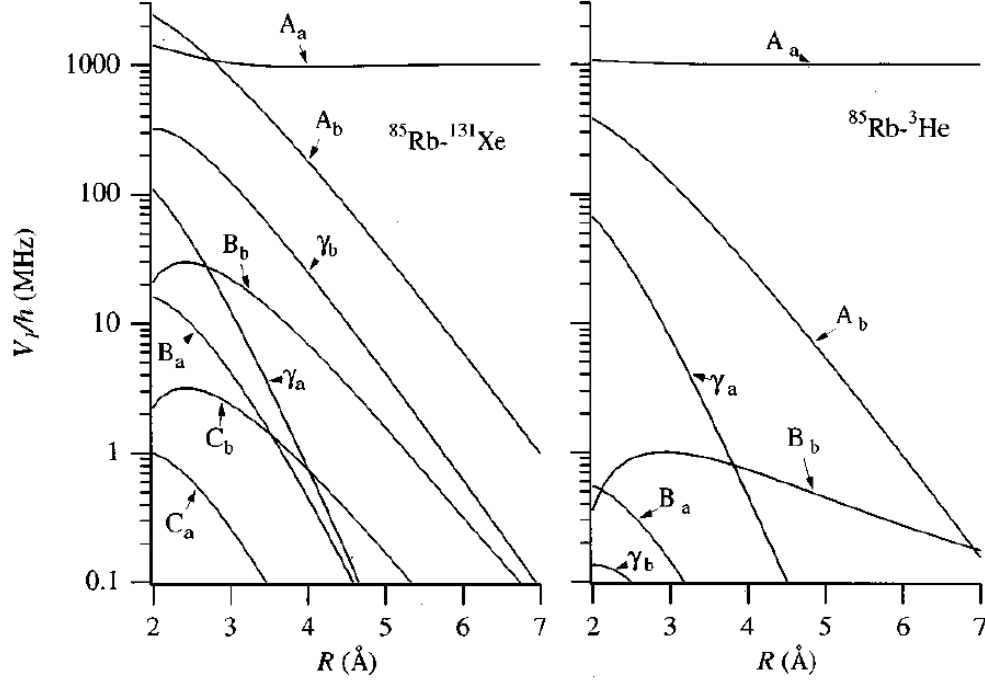


**Figure 1.7: Strengths of various spin-dependent interactions as functions of separation(from Ref. [?])**

where $\vec{I}_a$ and $\vec{I}_b$ are the nuclear spins of the atomic pair, where a stands for alkali metal atom and b stands for noble gas atom. $\gamma$ is the coefficient of the spin-rotation interaction, while $A_k$, $B_k$, $C_k$ are the coefficients for isotropic magnetic-

17

dipole hyperfine interactions, anisotropic magnetic-dipole hyperfine interactions, and electric quadrupole interactions, respectively. $A_a$ greatly exceed other coefficients as the separations between atoms increase.

The isotropic hyperfine interactions come from the Fermi-contact magnetic fields of the two nuclei. $A_b$ is the term responsible for spin exchange:

$$A_b(R) = \frac{8\pi g_s \mu_B \mu_b}{3I_b} |\eta \phi_0(R)|^2 \tag{1.24}$$

where $\eta$ is the enhancement factor which equals to the ratio of the perturbed wave function at the noble gas nucleus to that without the noble gas atom. The isotropic hyperfine interaction also introduces a frequency shift of the magnetic resonance lines for alkali-metal and noble gas atoms. The frequency shift is characterized by another enhancement factor $\kappa$ which is the ratio of the actual shift of the alkali metal electron lines due to the presence of polarized noble gas nuclei to what would be produced by the bulk magnetization of polarized noble gas. The shift is used in the technique Electron Paramagnetic Resonance (EPR) to calculate the polarization of noble gas nuclei.

The isotropic magnetic-dipole coupling polarizes the noble gas nuclei parallel to the electron spin polarization, while the anisotropic magnetic-dipole coupling polarizes in the opposite direction. Fortunately, the anisotropic interaction is negligible compared to isotropic interaction.

## 1.3.2 Spin Exchange Rate

The spin exchange rate due to binary collisions is:

$$\gamma_{se} = <\sigma_{se}v> [Rb] = k_{se}[Rb] \tag{1.25}$$

where $k_{se} = <\sigma_{se}v>$ is the velocity-averaged spin exchange rate constant. $k_{se}$ for spin exchange between $^3He$ and Rb is:

$$k_{se}^{^3He-Rb} = (6.7 \pm 0.7) \times 10^{-20} cm^3/s \tag{1.26}$$

Under 170°C which is a typical temperature that we run tests with,

$$[Rb] = 2.60 \times 10^{14} cm^{-3} \tag{1.27}$$

Thus for a single chamber cell,

$$\frac{1}{\gamma_{se}} \approx 15.9 hrs \tag{1.28}$$

## 1.4 $^3He$ Spinup and Relaxation

Similar to the optical pumping process of Rb, $^3He$ polarization can be described by

$$P_{^3He}(t) = P_0^{^3He} e^{-(\gamma_{se}+\Gamma)t} + P_\infty^{^3He}(1 - e^{-(\gamma_{se}+\Gamma)t}) \tag{1.29}$$

where the saturation polarization is

$$P_\infty^{^3He} = P_\infty^{Rb} \frac{\gamma_{se}}{\gamma_{se} + \Gamma} \tag{1.30}$$

And $\Gamma$ is the total relaxation rate of $^3$He nucleus spin polarization,

$$\Gamma = \Gamma_{dipolar} + \Gamma_{inhomogeneity} + \Gamma_{wall} \tag{1.31}$$

When a target cell are used in electron scattering experiments where an electron beam goes through part of the cell, an additional relaxation rate due to the beam $\Gamma_{beam}$ should also be included.

The coupling of nuclear spin to orbital angular momentum creates an intrinsic $^3$He relaxation rate that depends on density. At room temperature $(23°C)$, the dipolar relaxation rate is

$$\frac{1}{\Gamma_{dipolar}} = \frac{[^3He]}{744} hr^{-1} \tag{1.32}$$

where $[^3He]$ is the $^3He$ density in amagats. Assuming the cell density is 8 amg, the relaxation rate is $1/93\ hr^{-1}$. In addition, there is an additional intrinsic relaxation due to the spin-rotation interaction. This mechanism dominates the relaxation for $^{129}$Xe but is small for $^3$He.

The relaxation rate due to field inhomogeneities is

$$\Gamma_{inhomogeneity} = D\frac{|\nabla B_x|^2 + |\nabla B_y|^2}{B_0^2} \tag{1.33}$$

where D is the $^3$He diffusion constant, $\nabla B_x$ and $\nabla B_y$ are the transverse magnetic field inhomogeneities, $B_0$ is the holding field along z-axis. Under operating conditions, assuming the pressure is around 12 atm and field is 12.6 G, $D \approx 0.16 cm^2/s$ and the field inhomogeneities are 10mG/cm, the relaxation rate is 1/1400 $hr^{-1}$.

Wall relaxation is typically the dominant relaxation mechanism for cells in our lab. This mechanism depends on the property of the inner surface of glass. Most

of the target cells are contructed with reblown General Electric Type 180 (GE-180) glass. This aluminosilicate glass is highly impermeable to $^3$He. The wall relaxation is believed to be associated to several different mechanisms, such as paramagnetic impurities in the glass and microfissures in the surface that could trap $^3$He atoms. It has been found reblowing the glass can help lower the wall relaxation rate because it reduces the number of microfissures. The wall relaxation is not well understood, but it is believed to scale with the surface-to-volume ratio:

$$\Gamma_{wall} = \rho S/V \tag{1.34}$$

where $\rho$ is called relaxivity.

## 1.5   X Factor

In 2006, Babcok *et al.* reported evidence of a previously unrecognized spin relaxation mechanism, and named it X factor. This mechanism appears to be temperature dependent and roughly proportional to alkali density. The X factor limits the maximally achievable $^3$He polarization even with infinite laser power. The saturation polarization is

$$P_\infty^{^3He} = P_\infty^{Rb} \frac{\gamma_{se}}{\gamma_{se}(1 + X) + \Gamma} \tag{1.35}$$

In the presence of infinite laser power where $\gamma_{se} \gg \Gamma$, the saturation polarization becomes

$$P_\infty^{^3He} = P_\infty^{Rb} \frac{1}{1 + X} \tag{1.36}$$

21

# Chapter 2

# $^3$He Polarimetry

## 2.1  Overview

Traditional pure glass target cells are studied mainly using Adiabatic Fast Passage (AFP) Nuclear Magnetic Resonance (NMR) and Electron Paramagnetic Resonance (EPR). AFP is a technique that allows us to monitor a signal that is directly proportional to the $^3$He polarization, which serves as a means to gain knowledge of properties of cell including the time it takes to polarize it and the relaxation rates of its polarization. The EPR technique utilizes the fact that polarized $^3$He produces frequency shift of the magnetic resonance lines of alkali metal to measure the $^3$He polarization. When AFP and EPR are combined, we can calculate the calibration constant between an AFP signal and the corresponding $^3$He polarization.

A significant focus of my studies is on exploring cells that incorporate metal. Unfortunately, AFP is not suitable for studying these cells as it requires exposing the entirety of the cell to a Radio Frequency (RF) magnetic field in an attempt to flip all

spins in the cell. The RF field would induce an Eddy current induced in the metal body that significantly affects the resulting signal. For these cells, Pulsed Nuclear Magnetic Resonance (PNMR) has proven to be very useful. PNMR only applies a pulsed RF field to a small selected part of the cell which makes it relatively easy to prevent metal from distorting the signal. However, the spins tipped by applying the pulse lose their transverse component (which depends on the "tip angle"), we typically allow some time for this portion of gas to diffuse out of the region being monitored before we can the next measurement on a fresh sample of the gas. The highest rate at which PNMR measurements can be taken is limited by this requirement.

This chapter introduces the three techniques mentioned above and how they're used for our studies.

## 2.2   Adiabatic Fast Passage

### 2.2.1   Nuclear Magnetic Resonance

The energy of a magnetic moment in an external field is

$$E = -\vec{\mu} \cdot \vec{B_0} = -\mu_z B_0 \tag{2.1}$$

where $\vec{\mu}$ is the magnetic moment, for a spin-1/2 nuclei, the energy is

$$E = -\gamma B_0 \hbar/2 \tag{2.2}$$

$\gamma$ is the gyromagnetic ratio, $\gamma/2\pi \approx 3.2434 kHz/Gauss$. When a oscillating magnetic field with the frequency $\omega = \gamma B_0$ is present, transitions between the $+1/2$ and

-1/2 states are induced. This frequency is called Larmor frequency. When a nucleus is placed in an external magnetic field that is not aligned with its magnetic moment, it will precess at the Larmor frequency.

## 2.2.2 The Rotating Coordinate System

### 2.2.2.1 Classical Formulation

For a nucleus in an external field $\vec{B}$ with $\gamma \hbar \vec{I}$ as its nuclear angular momentum, the equation of motion in a stationary coordinate system is [?]

$$\hbar \frac{d\vec{I}}{dt} = \gamma \hbar \vec{I} \times \vec{B} \tag{2.3}$$

Let $\frac{\partial}{\partial t}$ represent the derivative with respect to a coordinate system that rotates with angular velocity $\vec{\omega}$,

$$\frac{d\vec{I}}{dt} = \frac{\partial \vec{I}}{\partial t} + \vec{\omega} \times \vec{I} \tag{2.4}$$

Substitute Eq. 2.4 into Eq. 2.3, $\vec{I}$ in the rotating frame satisfies the equation of motion

$$\hbar \frac{\partial \vec{I}}{\partial t} = \gamma \hbar \vec{I} \times (\vec{B} + \vec{\omega}/\gamma) = \gamma \hbar \vec{I} \times \vec{B}_{eff} \tag{2.5}$$

where $\vec{B}_{eff}$ is the effective field in the rotating frame

$$\vec{B}_{eff} = \vec{B} + \vec{\omega}/\gamma \tag{2.6}$$

Thus, the effective field experienced by an observer in the rotating frame is simply the external field $\vec{B}$ plus an additional field $\vec{\omega}/\gamma$.

If we apply this result to rotating magnetic fields, we will get the core idea of performing an Adiabatic Fast Passage (AFP) measurement. Assuming a constant field $\vec{B}$ and another field $\vec{B}_1$ perpendicular to $\vec{B}$ that is rotating with angular velocity $-\omega$. In the rotating frame that rotates with $\vec{B}_1$, both aforementioned fields are just constant and the effective field in the rotating frame is

$$B_{eff}\vec{z} = (B - \omega/\gamma)\vec{z} + B_1\vec{x'} \tag{2.7}$$

where $\vec{x'}$ is the direction that $\vec{B}_1$ is in. When on resonance ($B = \omega/\gamma$), the effective field is perpendicular to the constant field $\vec{B}$.

## 2.2.2.2 Quantum Mechanical Formulation

The above conclusion can be easily reached with quantum mechanics. The Shrödinger equation for a magnetic moment in an external field is

$$i\hbar\dot{\psi} = \mathcal{H}\psi = -\gamma\hbar\vec{I} \cdot \vec{B}\psi \tag{2.8}$$

Let $\psi$ and $\vec{B}$ be the wave function and magnetic field in a stationary frame and $\psi_r$ and $\vec{B}_r$ be the same quantities in a rotating frame with angular velocity $\vec{\omega}$. Using the rotation operator in quantum mechanics,

$$\psi = e^{-i\vec{\omega}\cdot\vec{I}t}\psi_r \tag{2.9a}$$

$$\vec{I} \cdot \vec{B}_r = e^{i\vec{\omega}\cdot\vec{I}t}\vec{I} \cdot \vec{B}e^{-i\vec{\omega}\cdot\vec{I}t} \tag{2.9b}$$

Substituting 2.9 into Eq.2.8, the Shrödinger equation in the rotating frame is obtained

$$i\hbar\dot{\psi}_r = -\gamma\hbar\vec{I} \cdot (\vec{B_r} + \vec{\omega}/\gamma)\psi_r = -\gamma\hbar\vec{I} \cdot \vec{B_{eff}}\psi_r \qquad (2.10)$$

The same effective field in the rotating frame is reached as that from the classical derivation.

### 2.2.3   Adiabatic Fast Passage

Adiabatic Fast Passage (AFP) NMR is used to measure the $^e$He polarization. In an AFP measurement, with the assistance of a oscillating radiofrequency (RF) field, the spins follow the effective field in a rotating frame (as discussed in more detail below) and are flipped 180 degrees to the opposite direction and then flipped back, producing two peaks in signal when they're perpendicular to the holding field and the pick up coils.
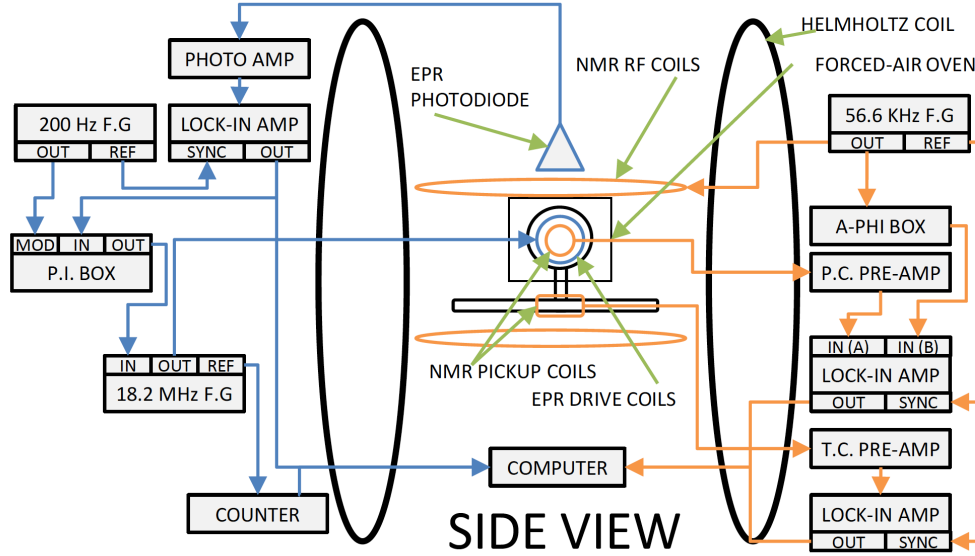
**Figure 2.1: EPR (left) and AFP (right) setup. Adapted from Dolph's PhD thesis.**

The flipping process can be achieved by either sweeping the main holding field or sweeping the RF frequency so that the longitudinal component of effective field in the rotating frame goes through zero. AFP measurements in out lab are typically done by sweeping the holding field while keeping the RF frequency constant. The RF coils produce a RF field of magnitude $2B_1$ perpendicular to the main holding field B. The oscillating field has a frequency of $\omega$ and can be decomposed into two counter-rotating components with the same amplitude $B_1$. Only the component rotating in direction able to give a resonance in Eq. 2.7 has an important effect. In this frame, the effective field is

$$B_{eff}\vec{z} = (B - \omega/\gamma)\vec{z} + B_1\vec{x'} \qquad (2.11)$$

27

as discussed above. The other rotating component that rotates in the opposite direction does not affect the spins. In an AFP measurement, the holding field starts from a value lower than $\omega/\gamma$ ($\omega/\gamma - B \gg B_1$), so that the effective field is almost aligned with the holding field and the spins. The holding field is then swept at a constant rate through resonance to a value greater than $\omega/\gamma$. The sweeping rate is of great importance. The sweep needs to be slow enough so that the nuclear spins can follow the effective field

$$\frac{\dot{B}}{B_1} \ll \omega \qquad (2.12)$$

Sweep that satisfies this condition is considered as adiabatic.

Sweep rate cannot be too slow either, because the relaxation rate of the spins are faster near the resonance especially with a small effective field $B_1$. The relaxation rate of $^3$He in the rotating frame at resonance is

$$\frac{1}{T_{1r}} = D\frac{|\nabla B_z|^2}{B_1^2} \qquad (2.13)$$

where D is the $^3$He self-diffusion constant. In order to keep the AFP loss low, it's important for the time scale that the spins stay close to resonance to be much shorter than $1/T_{1r}$:

$$D\frac{|\nabla B_z|^2}{B_1^2} \ll \frac{\dot{B}}{B_1} \qquad (2.14)$$

Typically, the field is swept from 12.6 Gauss to 20.4 Gauss in 6s, thus

$$\dot{B} = 1.3G/s \tag{2.15a}$$

$$B1 \approx 100mG \tag{2.15b}$$

$$f = 56.6kHz \tag{2.15c}$$

$$D \approx 0.16cm^2/s \tag{2.15d}$$

$$|\nabla B_z| \approx 10mG/cm \tag{2.15e}$$

$$\tag{2.15f}$$

With these operating conditions,

$$D\frac{|\nabla B_z|^2}{B_1^2} \approx 1.6mHz \tag{2.16a}$$

$$\frac{\dot{B}}{B_1} \approx 13Hz \tag{2.16b}$$

$$w \approx 356kHz \tag{2.16c}$$

The AFP conditions are clearly well satisfied. Fig.2.2 shows the evolution of effective field in the rotating frame during an AFP measurement.

**Before resonance**   **On resonance**   **After resonance**
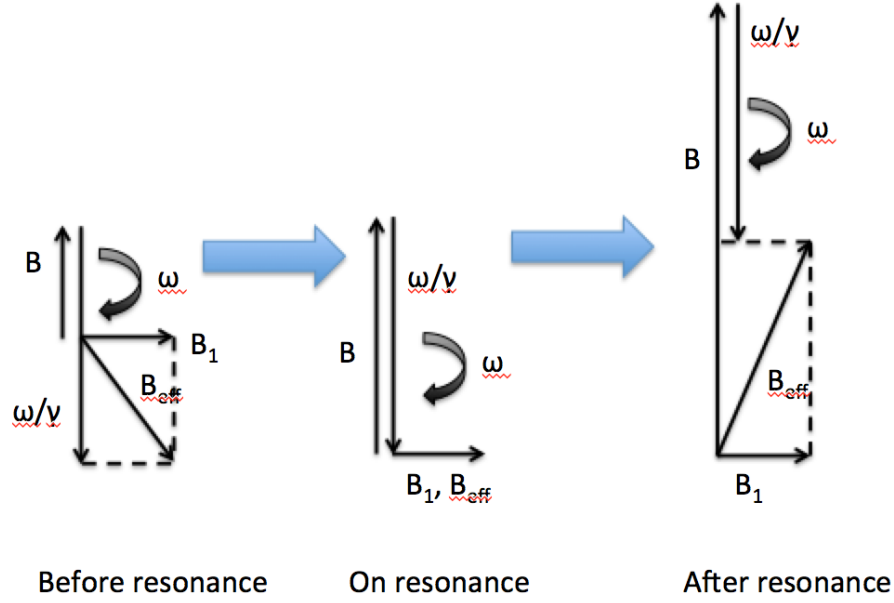
**Figure 2.2: Effective field in the rotating frame during an Adiabatic Fast Passage measurement. The $^3He$ spins follow the direction of the effective field. $B_1$ is exaggerated to show different components of effective field clearly.**

The pick up coils are placed close to the cell and perpendicular to the holding field and RF field. As the $^3$He spins precess along the holding field, the transverse component of the spins will induce an electromotive force (EMF) that is directly proportional to the amplitude of the component in the pick up coils. The signal can be written as:

$$S = A\omega \sin\alpha(t) = A\omega \frac{B_1}{\sqrt{B_1^2 + (B(t) - \omega/\gamma)^2}} \tag{2.17}$$

where A is a constant that accounts for the cell and coils geometry, the cell magnetization and the electronics factors that affect the size of signal; $\omega$ is the RF frequency; $\alpha$ is the angle between the effective field and the holding field in the rotating frame; B(t) is the holding field as a function of time. The signal reaches peak value when $B(t) = \omega/\gamma$. Fig.2.3 shows the result of a typical AFP measurement.
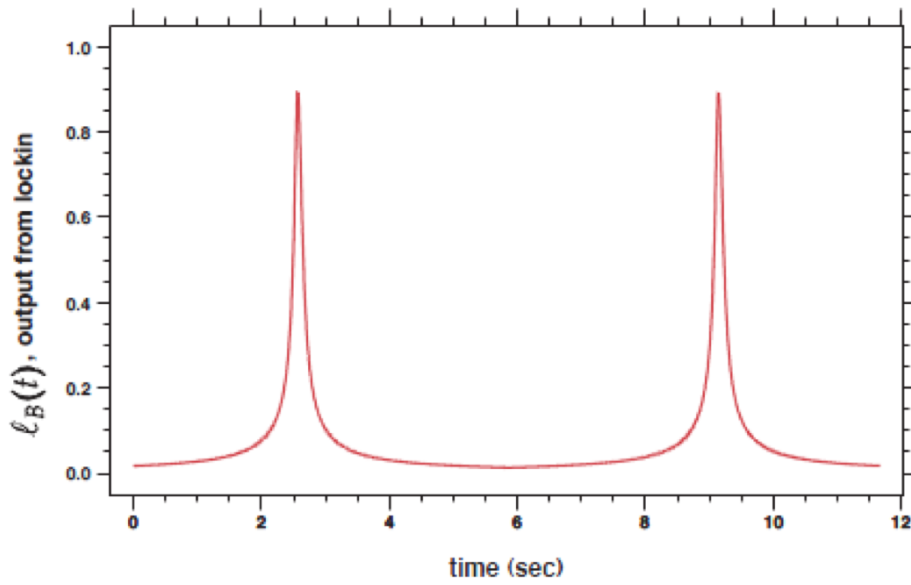


Figure 2.3: A typical AFP signal. y axis is in arbitrary unit.

### 2.2.4 AFP Loss

The longitudinal spin relaxation rate due to static field inhomogeneities is

$$\frac{1}{T_1} = D\frac{|\nabla B_x|^2 + |\nabla B_y|^2}{B_0^2} \tag{2.18}$$

where D is the diffusion constant for the polarized spins, and is inversely propor-

tional to the gas pressure. $B_0$ is the mean magnetic field along z axis. $B_x$ and $B_y$ are the x and y components of the magnetic field. However, when performing AFP measurement, the spins are exposed to a small oscillating RF field, the spin relaxation can be greatly accelerated under magnetic resonance conditions [?],

$$\frac{1}{T_{r1}} = \frac{8R^4}{175D}|\nabla\Omega_z|^2 \sum_n \frac{175}{4(\chi_{1n}^2 - 2)(\chi_{1n}^4 + r^2 + r^2 s^2)(1 + s^2)} \tag{2.19}$$

where R is the cell radius, D is the diffusion constant, $\Omega_z$ is the Larmor frequency of the holding field, $r = \frac{\omega_r R^2}{D}$, $s = \frac{\Omega_0 - \omega}{\omega_r}$, the numbers $\chi_{1n}$ are the zeros of the derivatives of the spherical Bessel functions

$$\frac{d}{dx}j_1(x_{1n}) = 0 \ for \ n = 1, 2, 3... \tag{2.20}$$

Since $r^2 \gg \chi_{1n}^4$, and $\sum_n \frac{1}{\chi_{1n}^2 - 2} = \frac{1}{2}$ [?],

$$\frac{1}{T_{r1}} = \frac{R^4|\nabla\Omega_z|^2}{r^2(1 + s^2)^2 D} = \frac{|\nabla B_z|^2 D}{B^2(1 + s^2)^2} \tag{2.21}$$

If $P_0$ is the polarization before AFP, the polarization P after a single AFP flip is given by

$$P = P_0 e^{-\int \Gamma_{r1} dt} = P_0 e^{-\int \frac{1}{T_{r1}} dt} \tag{2.22}$$

Given the field sweep starts from 12.6G, ends at 20.4G, the RF frequency is 56.6kHZ, the sweep time is 6s and $B_1$ is 100mG, we can safely approximate the integral by

$$\int_{-\infty}^{\infty} \frac{1}{T_{r1}} dt = \frac{\pi D |\nabla B_z|^2}{2B_1 \partial B_1 / \partial t} \tag{2.23}$$

which is the fractional loss due to a single AFP flip.

To better understand AFP loss, we performed a study where we took AFP measurements at various different field gradients to study the relation between AFP loss and inhomogeneities. The gradients were produced by Maxwell-style transverse gradient coils and increased from 0 to a little under 160 mG/cm. At each set gradient, we take one AFP to look at the difference between the two peaks to determine the loss due to a single flip. Fig 2.4 shows AFP losses collected from experiments and theoretical predictions. They agree mostly within the error bar.
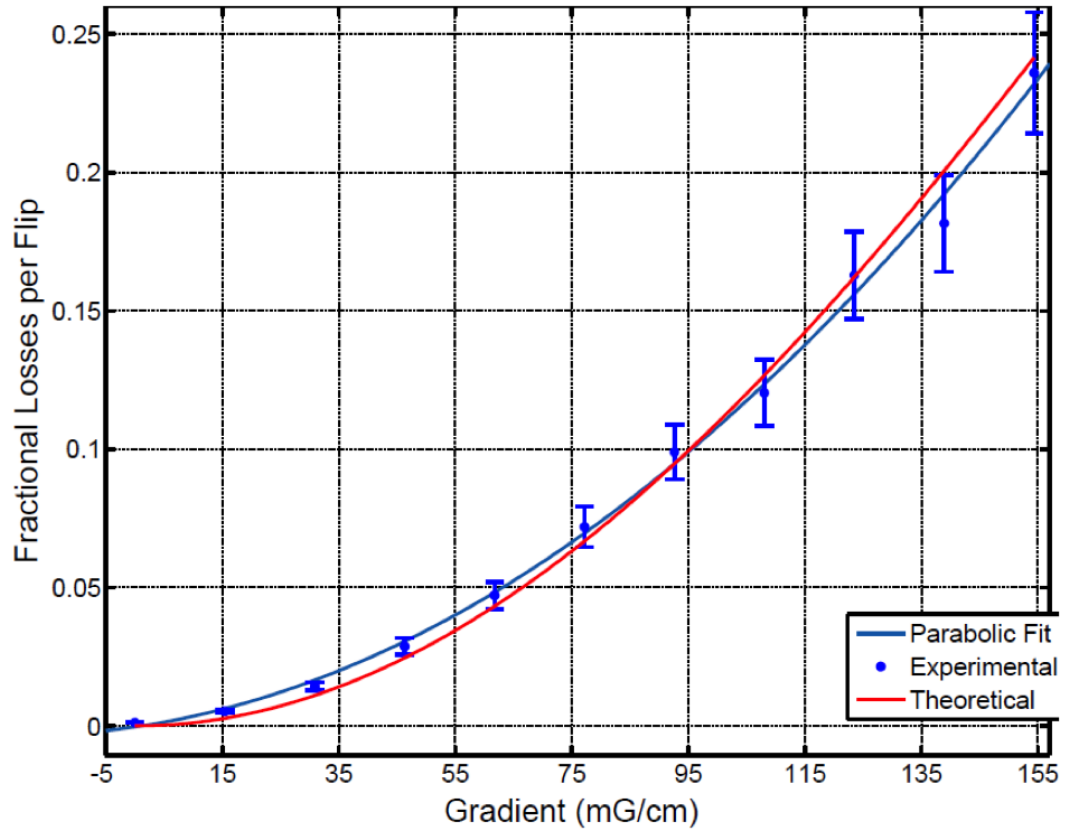


**Figure 2.4: Fractional AFP loss (single flip) as a function of field gradient.**

## 2.3 Electron Paramagnetic Resonance

### 2.3.1 Overview

Electron Paramagnetic Resonance (EPR) is a important technique for measuring the frequency shift of alkali metal Zeeman resonance due to the effective magnetic field produced by polarized $^3$He gas. The EPR shift is largely caused by the Fermi-contact interaction $\alpha\ \mathbf{K}\cdot\mathbf{S}$ between the nuclear spin $\mathbf{K}$ of the noble gas nucleus of magnetic moment $\mu_K$ and the electron spin $\mathbf{S}$ of the alkali metal atom [**?**]. The magnetic field created by the bulk magnetization of the $^3$He gas also contributes directly to a relatively small part of the shift (rougly 1/6 for K). The total measured shift is therefore written as the expected Zeeman interaction with the field produced by the polarized $^3$He multiplied by an enhancement factor $\kappa_0$. The enhancement effect comes from overlapping of alkali metal electrons and $^3$He nuclei during binary collisions, thus $\kappa_0$ is different for each alkali metal species and slightly temperature dependent.

During the process of optical pumping, the Rb atoms are excited to the $5P_{\frac{1}{2}}$ state by the pump laser. The majority of these atoms are quenched non-radiatively to the ground state by $N_2$. While at $5P_{\frac{1}{2}}$ state, Rb atoms can also be excited to the $5P_{\frac{3}{2}}$ state through collisions with other Rb atoms. A small fraction of the excited atoms ($5P_{\frac{1}{2}}$ and $5P_{\frac{3}{2}}$) decay by emitting either a $D_1$ photon or $D_2$ photon. The intensity of fluorescence is proportional to the excited Rb atoms, thus is higher when the Rb polarization is low so more Rb atoms can absorb laser and jump to the excited state. We typically induce Zeeman transitions with a RF coil to lower alkali polarization and detect $D_2$ photons with a photodiode behind a $D_2$ filter. The highest amount of $D_2$ photons is detected when the RF frequency is exactly equal to the Zeeman

transition frequency.

## 2.3.2 The Breit-Rabi Equation

The Zeeman energy levels of ground state (L = 0) can be described with the Breit-Rabi equation

$$E_{F=I\pm 1/2, m_F} = -\frac{h\Delta\nu_{hfs}}{2(2I+1)} - \mu_N g_I B m_F \pm \frac{h\Delta\nu_{hfs}}{2}\sqrt{1 + \frac{4m_F x}{2I+1} + x^2} \qquad (2.24)$$

where

$$x = (g_I \mu_N - g_s \mu_B)\frac{B}{h\Delta\nu_{hfs}} \qquad (2.25)$$

B is the magnetic field, $\Delta\nu_{hfs}$ is the hyperfine splitting frequency, I is the nuclear spin, $g_I$ and $g_s$ are the g factors of nuclear and electron spin, $\mu_N$ and $\mu_B$ are the nuclear and Bohr magneton, respectively.

The Zeeman transition frequency of $m_F \to m_F - 1$ is

$$\begin{aligned}
\nu_{m_F \to m_F-1} &= \frac{E_{F,m_F} - E_{F,m_F-1}}{h} \\
&= -\frac{g_I \mu_N B}{h} \pm \frac{\Delta\nu_{hfs}}{2}\left(\sqrt{1 + \frac{4m_F}{2I+1}x + x^2} - \sqrt{1 + \frac{4m_F-1}{2I+1}x + x^2}\right)
\end{aligned}$$
$$(2.26)$$

The second term is much greater than the first term under our operating conditions, so the sign of the frequency $\nu_{m_F \to m_F-1}$ depends on the second term only. If we focus on the top hyperfine manifold in the energy level graph, the transition frequency is

$$\nu_{m_F \to m_F-1} = -\frac{g_I \mu_N B}{h} + \frac{\Delta\nu_{hfs}}{2}\left(\sqrt{1 + \frac{4m_F}{2I+1}x + x^2} - \sqrt{1 + \frac{4m_F - 1}{2I+1}x + x^2}\right)$$

$$(2.27)$$

### 2.3.3 Shift of Zeeman Frequency

Under our operating condition, the size of Zeeman splitting is much less than hyperfine splitting, which makes x a small number. The Taylor expansion of Eq. 2.27 is

$$\nu_{m_F \to m_F-1} = -\frac{g_I \mu_N B}{h}$$
$$+ \frac{\Delta\nu_{hfs}}{2}\left(\frac{2x}{2I+1} - \frac{2(2m_F - 1)x^2}{(2I+1)^2} + \frac{(-(2I+1)^2 + 4 - 12m_F + 12m_F^2)x^3}{(2I+1)^3} + \cdots\right)$$

$$(2.28)$$

With the approximation

$$g_s \mu_B \gg g_I \mu_N \qquad (2.29a)$$

$$x \approx -\frac{g_s \mu_B B}{h \Delta\nu_{hfs}} \qquad (2.29b)$$

To the lowest order approximation, the shift of $\nu_{m_F \to m_F-1}$ due to a small effective field $\Delta B$ ($\Delta B \ll B$) from polarized $^3$He is

$$\Delta\nu_{m_F \to m_F-1} = -\frac{g_s \mu_B}{h(2I+1)}\Delta B\left[1 + 2(2m-1)\frac{g_s \mu_B B}{h\Delta\nu_{hfs}(2I+1)}\right.$$
$$\left. + 6\left(-\frac{(2I+1)^2}{4} + 1 - 3m + 3m^2\right)\left(\frac{g_s \mu_B B}{h\Delta\nu_{hfs}(2I+1)}\right)^2 + \cdots\right]$$

$$(2.30)$$

Usually the pumping chamber is spherical, the magnetic field produced inside a uniformly magnetized sphere is

$$\Delta \boldsymbol{B} = \frac{2}{3}\mu_0 \boldsymbol{M} \tag{2.31}$$

where $\mu_0$ is the vacuum permeability, $\boldsymbol{M}$ is the magnetization of $^3$He,

$$\boldsymbol{M} = \boldsymbol{\mu_K}[He]P \tag{2.32}$$

where $\mu_K$ is the magnetic moment of $^3$He, [He] is its density, and P its polarization. As we mentioned before, as a result of the Fermi-contact interaction $\alpha \mathbf{K} \cdot \mathbf{S}$ between the nuclear spin $\mathbf{K}$ of the noble gas nucleus and the electron spin $\mathbf{S}$ of the alkali metal atom, the effective magnetic field from the polarized $^3$He gas is enhanced by a factor of $\kappa_0$:

$$\Delta \boldsymbol{B} = \frac{2}{3}\kappa_0 \mu_0 \boldsymbol{\mu_K}[He]P \tag{2.33}$$

The enhancement factor $\kappa_0$ was measured by Romalis *et al.* in 1998 with an error of 1.5% [?]

$$\kappa_0^{Rb-^3He} = 4.52 + 0.00934[T(^\circ C)] \tag{2.34}$$

then it was measured by Babcock *et al.* in 2005

$$\kappa_0^{Rb} = 6.39 + 0.00914[T - 200(^\circ C)] \tag{2.35a}$$

$$\kappa_0^{K} = 5.99 + 0.0086[T - 200(^\circ C)] \tag{2.35b}$$

$$\kappa_0^{Na} = 4.84 + 0.00914[T - 200(^\circ C)] \tag{2.35c}$$

The two results agree within the error. Thus we can calculate $^3$He polarization with the EPR frequency shift.

## 2.3.4   Experimental Methods

### 2.3.4.1   Overview

Under normal operating conditions, hybrid cells with mixture of Rb and K are used. The vapor density of K is an order of magnitude higher than that of Rb, we typically induce the $m_F = 2 \rightarrow m_F = 1$ (assuming the angular momentum of laser photons is $+1$) $^{39}$K transition, which lowers the K polarization. Rb-K spin-exchange rate is fast enough that Rb is depolarized almost instantly. This allows more Rb atoms to absorb laser and be excited to the $5P_{\frac{1}{2}}$ state which in turn produces more $D_2$ fluorescence. The $D_2$ fluorescence is at maximum intensity when the RF frequency is on resonance for the Zeeman transition.

We first locate the frequency with a frequency-modulated (FM) sweep, and set the RF frequency to the found value. The RF is locked to the frequency (which is slightly changing) that induces maximum $D_2$ light with a proportional-integral feedback circuit (P.I. box). This frequency is referred to as EPR frequency and is measured with a counter. To separate the frequency-shifting effect of polarized $^3$He from other sources

that may affect the transition frequency, we flip the ${}^3$He magnetization by perform-
ing a RF frequency sweep. A frequency sweep is chosen rather than a holding field
sweep to keep external magnetic field constant, thus reducing factors that affect Zee-
man splitting size. By comparing the frequency measured before and after the flip,
together with the real temperature inside the pumping chamber, we can calculate
the ${}^3$He polarization. We typically take AFP measurements right before and after
the relatively quick EPR measurement, so that a calibration constant that translates
AFP signal size to ${}^3$He polarization can be calculated.

### 2.3.4.2   Locating Zeeman Transition Frequency

The P.I. box only works well in locking the EPR frequency to the $m_F = 2 \rightarrow m_F = 1$
K transition when the EPR frequency is close to the transition. Thus the first step in
EPR measurements is to locate the Zeeman transition. A frequency-modulated (FM)
sweep is performed through a range that covers the Zeeman transition, the range is
known from experience or calculation and the P.I. box remains off during the sweep.

The RF frequency is generated by the 18.2MHz voltage-controlled oscillator (VCO).
The D$_2$ fluorescence is detected with the photodiode and recorded during the sweep.
The RF is frequency-modulated by a 200Hz signal, the VCO output at any moment
during the sweep can be described as:

$$V_{FM}(t) = V_{C0} \sin\left(2\pi[f_c + D_f \sin\left(2\pi f_m t + \phi_m\right)]t + \phi_c\right) \tag{2.36}$$

where $V_{C0}$ is the amplitude of the sweeping RF frequency (carrier), $f_c$ is the RF
frequency that is being swept through a set range, $D_f$ is the peak frequency deviation,
$f_m$ is the modulating frequency (200Hz in our case), $\phi_m$ and $\phi_c$ are the phase of the

modulation frequency and carrier frequency, respectively. Thus the RF frequency is

$$f_{FM}(t) = f_c(t) + D_f \sin\left(2\pi f_m t + \phi_m\right) \tag{2.37}$$

here $f_c(t)$ emphasizes the RF frequency is sweeping over time.

The $D_2$ light intensity can be described with a Lorentzian function:

$$I(f(t)) = \frac{I_0}{(f_{FM}(t) - f_0)^2 + \Gamma^2} \tag{2.38}$$

where $f_0$ is the Zeeman transition frequency, $\Gamma$ is the line width. Keeping the first order term of the Taylor expansion of Eq. 2.38, the $D_2$ light intensity is

$$I(f(t)) = I(f_c(t)) + \left. \frac{\partial I}{\partial f} \right|_{f=f_c(t)} D_f \sin\left(2\pi f_m t + \phi_m\right) \tag{2.39}$$

A lock-in amplifier is used to select only the $f_m$ term and reduce the noise, the signal picked by the lock-in is

$$s(t) = \left. \frac{\partial I}{\partial f} \right|_{f=f_c(t)} D_f \sin\left(2\pi f_m t + \phi_m\right) \tag{2.40}$$

which is the derivative of the Lorentzian function multiplied by a sine function. The FM sweep line crosses zero when the RF frequency is equal to the Zeeman transition frequency (peak of the Lorentzian function), which produces the maximum $D_2$ light intensity. The region between the lowest and highest points of the derivative line is fitted to a line, and the zero-crossing point of the line is used as the Zeeman transition frequency. Fig. 2.5 shows an FM sweep.
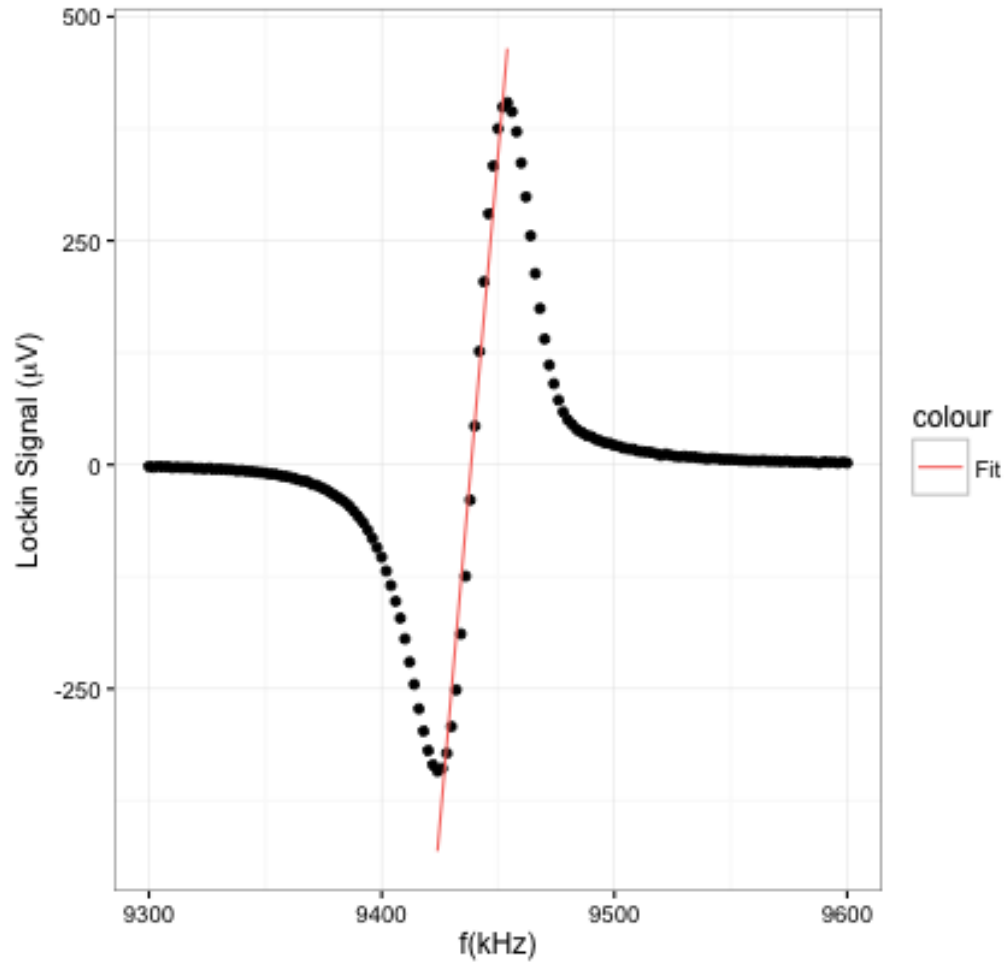
**Figure 2.5:** A typical FM sweep on a hybrid cell. The central region between the minimum and maximum is fitted to a line. The zero crossing point corresponds to the Zeeman transition frequency.

### 2.3.4.3   EPR Spin Flip Process

After the transition frequency is located, the VCO frequency is first set to it and then stays locked with a proportional-integral feedback circuit (P.I. box). The circuit is shown in Fig. 2.6.

The output of the lock-in amplifier is sent to the input of the P.I. box, and the
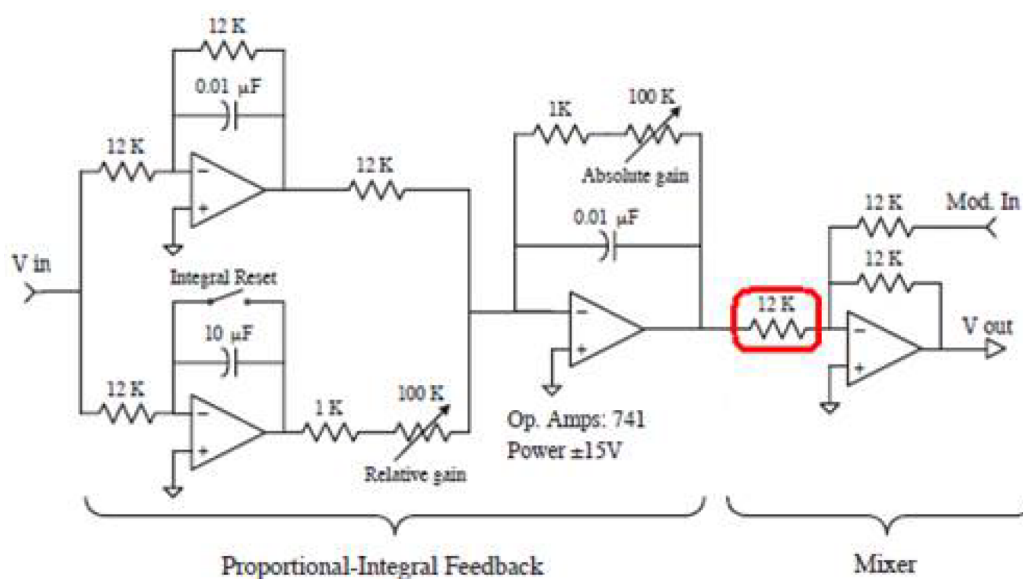
**Figure 2.6: The same P.I. circuit that was first used by Romalis in our lab. The drawing was then corrected by Peter Dolph.[?]**

output of the P.I. box controls the input of the VCO. If the effective magnetic field drifts away from resonance, the P.I. box would receive a non-zero input, and attempt to change the frequency of the VCO output so that its input is zero again. Therefore, the VCO output always matches the transition frequency.

Because the EPR frequency is also affected by sources other than the polarized $^3$He such as the holding field and earth field, we flip the $^3$He spins by sweeping the frequency while keeping the holding field unchanged. The contribution from the flipped spins has a opposite sign while other factors still contribute in the same way which allows us to extract the change of Zeeman transition frequency due to polarized $^3$He and calculate the polarization. We typically let the cell polarization reach saturation before performing EPR measurements. AFP measurements are taken right before and after the EPR measurements for calculating the calibration constant
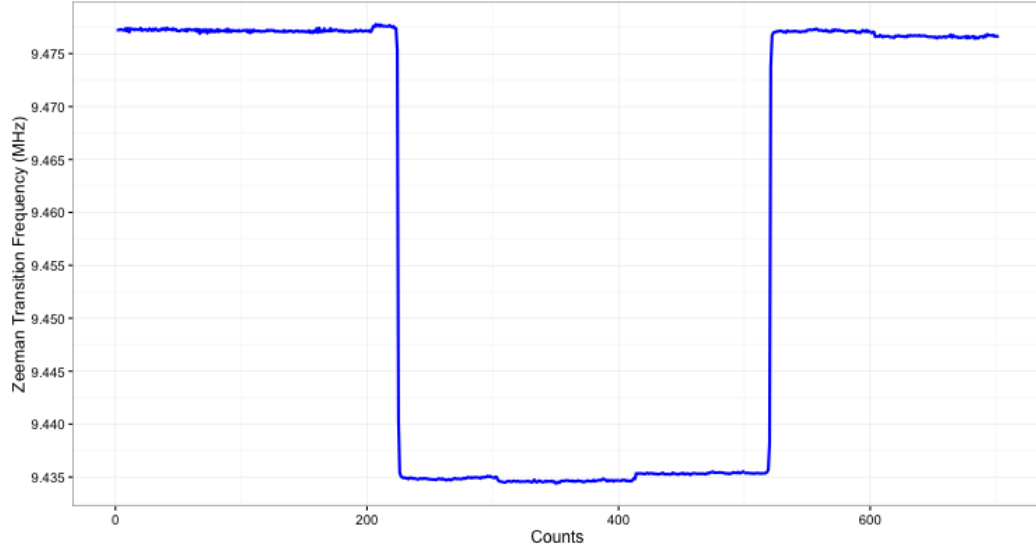
**Figure 2.7: An EPR measurement for a hybrid cell at 235°C.**

The spins are flipped around 200 mark, and flipped back around 500 mark.

(the ratio between polarization and AFP signal size). Fig. 2.7 shows a typical EPR spin flip process.

Under normal operating conditions for a double-chambered cell, the pumping chamber is heated to around 170°C or 235°C depending on if the cell is hybrid, the target chamber and transfer tube remain at room temperature. The temperature difference causes differences in gas densities and affects AFP signal size. Temperature controller of the oven only maintains the surface temperature of the pumping chamber at set temperature, but the gas inside the pumping chamber is always hotter due to absorption of laser energy. The enhancement factor $\kappa_0$ is also slightly temperature dependent which may be underestimated by $\sim 4\%$ when using the surface temperature as the gas temperature. Dolph described a method called temperature test to extract gas temperature inside the pumping chamber in detail in his thesis [**?**]. The idea is to take AFP measurements when the laser is blocked and unblocked multiple times,

assuming the change of gas densities due to absorption of laser is the only reason for the difference in signal size (aside from AFP loss which is compensated through fitting) and the gas temperature when laser is blocked is the same as that measured by RTDs (resistance temperature detectors) on the exterior of the pumping chamber, one can calculate the inside temperature when laser is unblocked.

## 2.4    Pulsed Nuclear Magnetic Resonance

Adiabatic Fast Passage has been the main technique used in our lab for measuring $^3$He polarization through detecting precessing spins with detection coils (we refer to them as pickup coils). In an AFP measurement, all $^3$He spins are flipped by sweeping the holding field while applying a RF field. In more recent studies, we have been exploring the possibility of replacing conventional glass windows with metal end windows in response to the 12 GeV upgrade of JLab. Because of the lack of studies on spin relaxation of polarized $^3$He on metal surfaces, various test cells made with large metal parts as well as glass parts are being studied in our lab. The inclusion of metal parts immediately renders AFP almost useless in the situation because of effects such as Eddy current, thus we have been performing Pulsed Nuclear Magnetic Resonance (PNMR) on metal cells.

### 2.4.1    The Rotating Coordinate System

In a PNMR measurement, a short pulse of RF frequency is applied to a small fraction of $^3$He gas. The RF frequency is tuned to be on resonance at the Larmor frequency of the holding field. As discussed before with AFP, in the rotating coordinate system,

there will be an effective field due to rotation that exactly cancels the holding field which we assume to be in the z direction. Thus the z component of the effective field is zero and there is a non-zero constant transverse component which we will call $B_1$. The nuclear spins will precess along $B_1$ and end up at an angle away from z axis:

$$\alpha = \gamma B_1 \Delta t \tag{2.41}$$

where $\alpha$ is the angle (tip angle), $\gamma$ is the gyromagnetic ratio, and $\Delta t$ is the RF pulse duration.

### 2.4.2 Free Induction Decay

At the end of the RF pulse, the tipped spins will have a transverse component equal to the magnetization multiplied by $\sin \alpha$. The spins continue to precess along the holding field and the transverse component will induce a signal in the pickup coils.

In addition to precession, the spins are affected by two types of relaxation processes. The first type is called the spin-lattice relaxation, it describes the rate at which the longitudinal component of magnetization approaches the thermodynamic equilibrium value. It is characterized by the spin-lattice relaxation time constant $T_1$. The rate of change of the longitudinal component is

$$\dot{M_z} = -(M_z - M_0)/T_1 \tag{2.42}$$

where $M_0$ is the thermodynamic equilibrium magnetization. Solving the differential equation gives

$$M_z(t) = M_0 - [M_0 - M_z(0)] \, e^{-t/T_1} \tag{2.43}$$

The name spin-lattice relaxation refers to the process in which the spins transfer energy to surrounding, thereby restoring their equilibrium state.

The second relaxation process is the transverse relaxation, which is also referred to as the $T_2$ relaxation and spin-spin relaxation. The transverse component of magnetization decays because variations in the local magnetic field cause different moments to precess at different rates. This is the $T_2$ process. Normally, the dominating relaxation effect however, is another dephasing process due to inhomogeneities in the holding field over the volume of the cell.

The measured relaxation rate of the tipped spins is the result of all these effects combined:

$$\frac{1}{T_2^*} = \frac{1}{T_2} + \gamma \Delta B_0 \tag{2.44}$$

where $\Delta B_0$ is the variation in the holding field. $\gamma \Delta B_0$, the dominant term, is a spread in Larmor frequencies $\Delta \omega_0$, which causes spin-spin dephasing in a characteristic time of $1/\Delta \omega_0$.

The time evolution of the nuclear magnetization $\mathbf{M}$ is described by the Bloch equations [?]:

$$\frac{\partial M_x(t)}{\partial t} = \gamma \left( \boldsymbol{M}(t) \times \boldsymbol{B}(t) \right)_x - \frac{M_x(t)}{T_2^*} \qquad (2.45\text{a})$$

$$\frac{\partial M_y(t)}{\partial t} = \gamma \left( \boldsymbol{M}(t) \times \boldsymbol{B}(t) \right)_y - \frac{M_y(t)}{T_2^*} \qquad (2.45\text{b})$$

$$\frac{\partial M_z(t)}{\partial t} = \gamma \left( \boldsymbol{M}(t) \times \boldsymbol{B}(t) \right)_z - \frac{M_z(t)}{T_1} \qquad (2.45\text{c})$$

where $\gamma$ is the gyromagnetic ratio and the cross products are the precession terms, the last terms in each equation represent the decaying and dephasing of each component. The precessing spin magnetization generates a signal in the pickup coils that decays with time. This is called free induction decay, the induced signal is of the shape:

$$V(t) = A\omega_0 \sin \alpha \sin (\omega_0 t + \phi) e^{-t/T_2^*} \qquad (2.46)$$

where A is just a constant, $\omega_0$ is the Larmor frequency for the holding field, $\alpha$ is the tip angle, $T_2^*$ is the measured decay time constant. For our metal test cells, depending on the location of the pickup coils and the field setup, $T_2^*$ varies between several milliseconds to more than 300 milliseconds.

### 2.4.3 Experimental Methods

Our PNMR setup is shown in Fig. 2.8. The Labview program on the computer controls the timing of a gate signal that is fired from the first function generator. The gate signal is fed to the back of the second function generator and triggers it to produce a short pulse. The second function generator sends out RF pulse with pre-set amplitude, duration and frequency only when the gate signal is of voltage higher than
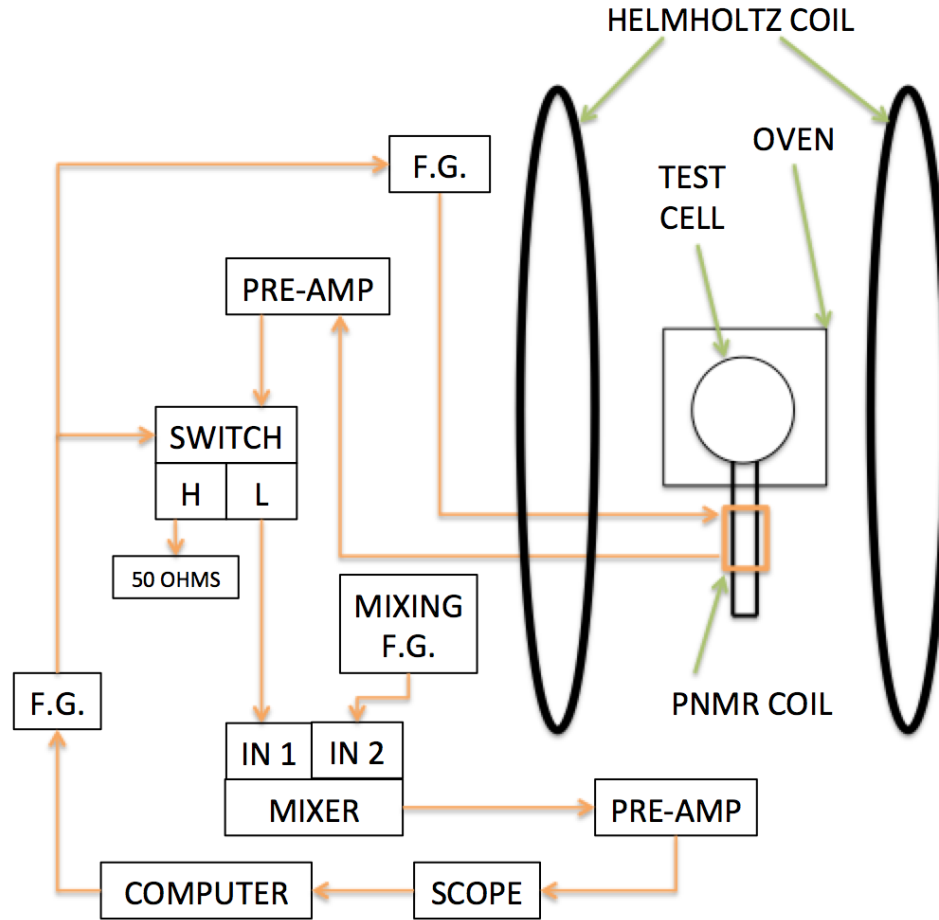
Figure 2.8: PNMR setup.

the threshold. The frequency of the RF pulse is carefully tuned to be at the Larmor frequency of the holding field.

The pulse is sent from the function generator to a coil wrapped directly on a small portion of the cell. The spins contained in the coil are exposed to the pulse and tipped by an angle which depends on the amplitude and the duration of the pulse. In the rotating frame, the effective field $B_1$ causes the spins to precess around it (as discussed before), the precession frequency is $\gamma B_1$ so the angle the spins rotate by

(tip angle) is

$$\alpha = \gamma B_1 \Delta t \tag{2.47}$$

where $\gamma$ is the gyromagnetic ratio, the effective field $B_1$ is directly proportional to the amplitude of the RF pulse, $\Delta t$ is the duration of the pulse. Ideally, a 90° tip angle would result in the maximum signal, but it has not been the case for us most of the time because of field inhomogeneities. The coils are normally wrapped on the transfer tube of the cell which is off the center of the holding field and exposed to greater inhomogeneities. The details of how we measure the test cells will be discussed in later chapters. Relatively large inhomogeneities cause the spins to precess at different rates, and the dephasing becomes more significant with longer pulse duration and larger tip angle, which leads to non-optimal signal. A typical tip angle for us would be between 30° and 45°.

After the spins are tipped away from z axis, they precess around the holding field and induce a signal in the detection coil. The signal is amplified by a low noise pre-amplifier first and then goes through an isolation switch. The switch only lets signal pass when the controlling gate voltage is low, thus stops the RF pulse from coming back through the detection circuit. The signal is at the Larmor frequency, and is mixed with another frequency after the switch. The mixing frequency is only slightly different from the Larmor frequency, the output of the mixer has both the sum of the two frequencies and the difference. A second pre-amplifier is used to select and amplify the lower of the two frequencies while filtering out high frequency noises. The final output is displayed on a oscilloscope and collected by the Labview program on

the computer. Fig. 2.9 shows a PNMR measurement with around 150 ms decay time constant.
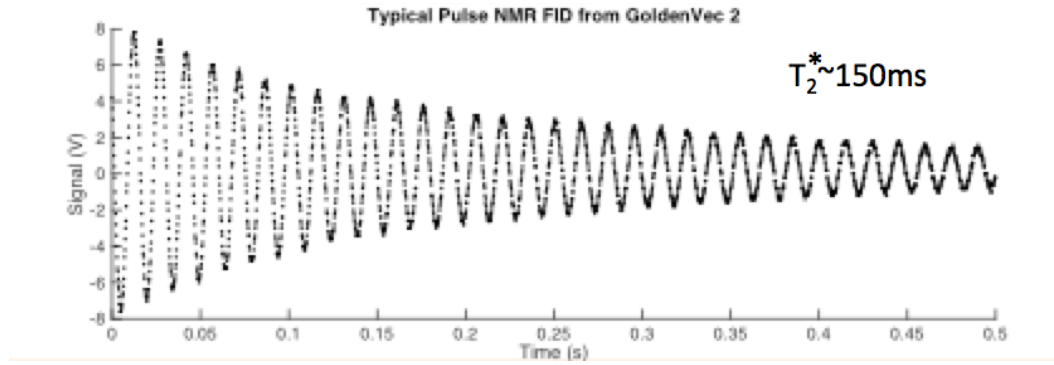


**Figure 2.9: A PNMR signal taken with gold coated test cell.**

The tip angle can be measured with a short sequence of FID signals. Theoretically the tip angle can be calculated with Eq. 2.47. But because of inhomogeneities and other factors, the calculation serves as only an estimate, it is often more accurate and convenient to measure the tip angle directly. We take several PNMR measurements in quick succession with the same RF pulse settings. After every pulse, the transverse component of the spins quickly decay and dephase, leaving only the longitudinal component which is equal to $\cos \alpha$ times the original magnetization. The intervals between measurements are short enough so that $T_1$ can be safely ignored. The series of measurements also need to be performed on the same portion of the gas (i.e. the same group of spins tipped by the first pulse), thus it is important to know that the self-diffusion of $^3$He is significantly slower than the sampling rate. The self-diffusion coefficient of $^3$He at 300K is [**?**]

$$D = \frac{1440(80)torr}{P}cm^2/s \tag{2.48}$$

which is roughly 1.89 cm$^2$/s at 760 torr (the test cells normally contain around 1 atm of $^3$He). The diffusion length is described by

$$l = 2\sqrt{Dt} \tag{2.49}$$

Thus in one second, the gas will move around 2.75 cm through self-diffusion. For this reason, we only take 2 or 3 PNMR measurements to calculate the tip angle. As additional measurements would have given enough time for the tipped spins from the first PNMR and the surrounding spins to mix.

Since only the longitudinal component of the tipped spins are preserved, the amplitude of the $i_{th}$ PNMR is

$$V_i = V_0 cos^{i-1}\alpha \tag{2.50}$$

where $V_0$ is the induced signal in the first PNMR. We can then use this equation to calculate the tip angle $\alpha$.

# Chapter 3

# Development of Hybrid Targets

## 3.1 Overview

In this chapter, I present the development of high-performance polarized $^3$He targets for use in electron scattering experiments that utilize the technique of alkali-hybrid spin-exchange optical pumping. Data of 24 separate target cells are presented, each of these cells was constructed while preparing for one of four experiments at Jefferson Laboratory. The results document dramatic improvement in the performance of polarized $^3$He targets. I focus on the data analysis work in this chapter since most of the data had already been taken by the time I joined the group. Other details are described by Jaideep Singh [?]. With the wide range of data, we successfully determined the so-called X-factors that quantify an as-yet poorly understood spin-relaxation mechanism that limits the maximum achievable $^3$He polarization to well under 100%. The data collected also served as a measurement of the K-$^3$He spin-exchange rate coefficient $k_{se}^K = (7.46 \pm 0.62) \times 10^{-20}$ cm$^3$/s over the temperature

range 503 K to 563 K.

## 3.2 Development of Hybrid Targets

Spin-exchange optical pumping (SEOP) is a two step process in which an alkali-metal vapor is polarized with optical pumping which subsequently polarizes noble-gas nuclei via spin-exchange collisions. A pure Rb vapor was used to polarize $^3$He prior to the development of hybrid cells. However, it was found that K is far more efficient than Rb at transferring its polarization to $^3$He nuclei. Hybrid mixtures of Rb and K were used more and more frequently to improve the efficiency of the polarization process. In alkali-hybrid spin-exchange optical pumping (AHSEOP), the Rb vapor is polarized by circularly polarized laser, but the polarization of Rb valence electrons is then rapidly shared with the K. The rate at which Rb and K exchange polarization is so fast that their polarizations can be thought of as being equal. If the alkali-hybrid mixture contains significantly more K than Rb with appropriate ratio, the spin-exchange efficiency is greatly improved so that the rate at which $^3$He is polarized is increased significantly for a given amount of laser power.

The second factor that proved to have improved target cells performance greatly was the use of spectrally-narrowed diode lasers. We were able to achieve higher alkali polarization with the aid of these lasers, which in turn reduced the required laser power. The origins of the improved cell performance are twofold. Firstly, these narrowband lasers have spectral profiles closely match the Rb $D_1$ absorption line shapes, which results in higher optical pumping rates and hence higher alkali polarizations. Secondly, it allows us to use higher alkali densities (which increases spin-exchange

rates) without sacrificing alkali polarization.

The data collected over the years include $^3$He polarization achieved under different operating conditions, the time constants of polarization process, the geometric properties of the target cells, and cell fill information such as pressure and ratio of K to Rb in hybrid mixtures, the time constants of spin relaxation process. In roughly half the cells, the alkali polarization and alkali density were also measured with Faraday rotation techniques. The results contain several thousand hours worth of data and provide valuable information for future cell development.

Two figures of merit (FOMs) are plotted in Fig. 3.1, both of which are relevant in evaluating the performance of a polarized $^3$He target. The one on the left axis is the effective luminosity $\mathcal{L}^{eff} = \mathcal{L}P_{He}^2$, where $\mathcal{L}$ is the luminosity for a fixed-target experiment (the product of beam current, target density, and interaction length) and $P_{He}$ is the $^3$He polarization. The luminosity $\mathcal{L}$ represents the number of scattering opportunities per unit time per unit area, while $P_{He}^2$ accounts for the reduction in statistical error of some polarization-dependant asymmetry. The FOM on the right axis is used to quantify the potential effective luminosity of a target. The definition is $\mathcal{L}^N = \mathcal{N}\Gamma_s P_{He}^2$, where $\mathcal{N}$ is the total number of $^3$He atoms in the target, $\Gamma_s$ is the rate at which polarization builds up. The target cell Antoinette is the first one with such high value of $\mathcal{L}^N$, which indicates tis cell could tolerate higher luminosities than previously achieved. The high potential further demonstrates the importance of the development of the new convection style target cell [?]. With even higher luminosities in electron scattering experiments, significantly faster gas transfer becomes quite necessary to reduce the polarization gradient between the pumping chamber of target chamber.
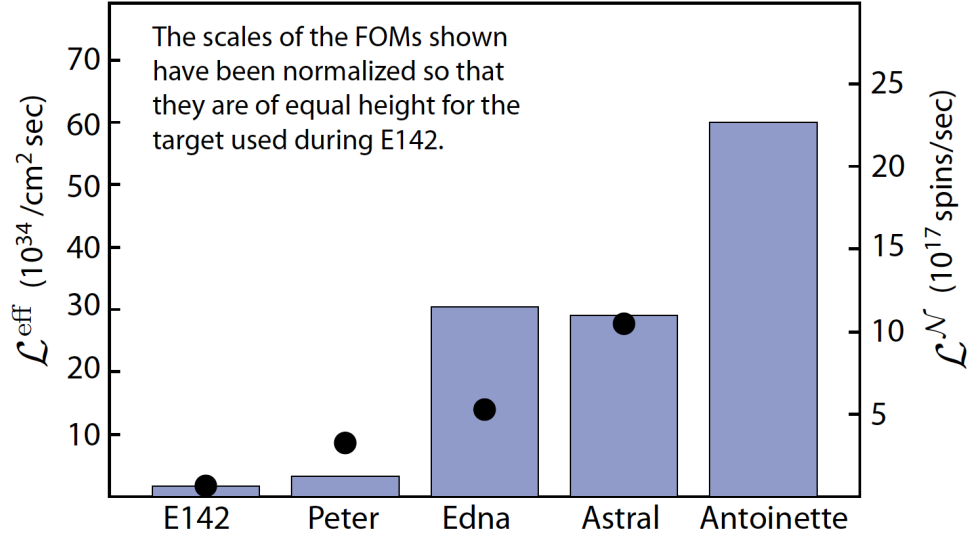
**Figure 3.1:** Shown are two figures of merit (FOM) for targets built for the indicated experiments. The circles (left axis) indicate the luminosity weighted by the square of polarization. The bars (right axis) represent the total number of spins being polarized per second weighted by the square of polarization. While the right FOM is an indication of the potential of the polarization technique, the left FOM indicates performance achieved during an experiment. The scales have been normalized so that the two FOMs have the same height for the cell marked E142

## 3.2.1 Experimental Methods

### 3.2.1.1 The $^3$He Targets

Chapter 2 has already described single-chambered cell polarization dynamics to some extent as it is a simpler model for introducing spin-exchange optical pumping. The $^3$He target cells JLab uses for electron scattering experiments usualy include two chambers, a pumping chamber (PC), which is placed in an oven and pumped by

circularly polarized laser, and a target chamber (TC) that the electron beam passes through. Fig.3.2 shows a typical cell.

Laser

Pumping Chamber (PC)

Transfer Tube (TT)

Electron Beam

Target Chamber (TC)
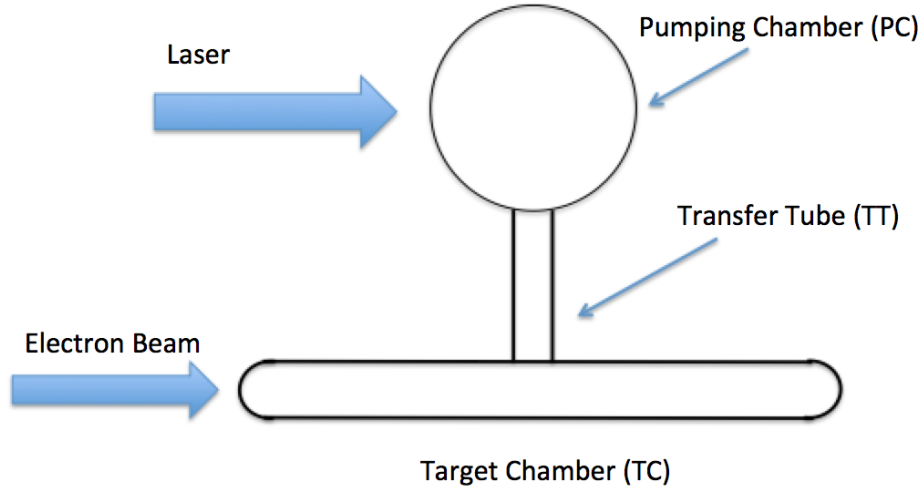
**Figure 3.2: A target cell. The dimensions of different parts of the cell are not to scale.**

After baking the cell to remove moisture and other contaminants, mixtures of Rb and K are chased into the cell. Once the cell has been pumped with a diffusion pump for about a week, we can fill the cell with $N_2$ and $^3$He.

The $^3$He density is of great importance for characterizing the target cells. One way to determine the $^3$He density is through measurements during the cell-filling process. A carefully calibrated volume, together with pressure and temperature measurements gives the volume of different spaces in the gas system (the system that is used to pump the cell and fill it with $N_2$ and $^3$He) and the cell. By comparing the amount of $^3$He

left in the system, the amount that went into the cell is obtained. The volume of the cell can be measured by determining its buoyancy force in water. The $^3$He density is determined to within about 1% with the method.

Another method used quite often for determining the $^3$He density is through measurements of the pressure broadening of the $D_1$ and $D_2$ absorption lines with a scannable single-frequency laser. This measurement also provides the value of D, which is the ratio of K vapor density to Rb vapor density. Although the value of D is for the temperature at which the measurement is performed, its value for operating condition can be inferred with alkali-metal vapor pressure curves. D is also measured with the Faraday rotation technique in many cases, and the two methods agree with each other quite well. The fill densities and geometric properties of the aforementioned 24 cells are shown in Table 3.1.

### 3.2.1.2 Target Cell Polarization Dynamics

As previously mentioned, AFP is used to monitor the polarization of $^3$He. An exact value of polarization remains to be calibrated with EPR, but the signal size is directly proportional to the polarization, thus is an indication of how the polarization changes relatively. Two processes that are monitored with AFP are spinups and spindowns.

The process of $^3$He gaining polarization through spin-exchange with Rb that is being constantly pumped by circularly polarized laser is called a spinup. A typical example of a spinup is shown in Fig. 3.3.

| EXP | Cell | Total Volume(cc) | PC Volume(cc) | Fill Density(amg) | TC length(cm) |
|---|---|---|---|---|---|
| saGDH | Proteus | 235.9 | 90.8 | 6.88 | 34.3 |
| | Peter | 208.6 | 111.3 | 8.80 | 39.4 |
| | Penelope | 204.3 | 102.2 | 8.93 | 39.7 |
| | Powell | 213.3 | 111.6 | 8.95 | 40.5 |
| | Prasch | 257.7 | 114.5 | 6.94 | 35.3 |
| GEN | Al | 168.4 | 90.2 | 8.91 | 38.4 |
| | Barbara | 386.2 | 306.8 | 7.60 | 38.7 |
| | Gloria | 378.2 | 298.8 | 7.40 | 38.4 |
| | Anna | 386.8 | 303.7 | 8.09 | 38.7 |
| | Dexter | 181.4 | 99.3 | 9.95 | 38.7 |
| | Edna | 378.3 | 290.3 | 7.47 | 38.7 |
| | Dolly | 378.3 | 293.5 | 7.42 | 38.7 |
| | Simone | 219.5 | 118.6 | 8.17 | 37.9 |
| | Sosa | 388.8 | 304.7 | 7.96 | 38.7 |
| Transversity and $d_2^n$ | Boris | 246.1 | 166.1 | 8.08 | 38.4 |
| | Samantha | 259.0 | 176.9 | 7.97 | 38.4 |
| | Alex | 278.3 | 193.9 | 7.73 | 39.1 |
| | Moss | 269.8 | 184.7 | 7.92 | 38.7 |
| | Tigger | 271.7 | 186.9 | 7.81 | 38.7 |
| | Astral | 251.4 | 164.9 | 8.18 | 38.4 |
| | Stephanie | 244.3 | 164.9 | 8.10 | 38.5 |
| | Brady | 249.9 | 169.3 | 7.88 | 38.4 |
| | Maureen | 268.5 | 177.4 | 7.63 | 39.8 |
| | Antoinette | 437.8 | 351.8 | 6.57 | 40.3 |

**Table 3.1:** The table contains the names, total and pumping chamber volumes, fill densities and target chamber lengths of the 24 target cells. The fill densities are the average of the results from gas system measurements and pressure broadening measurements.
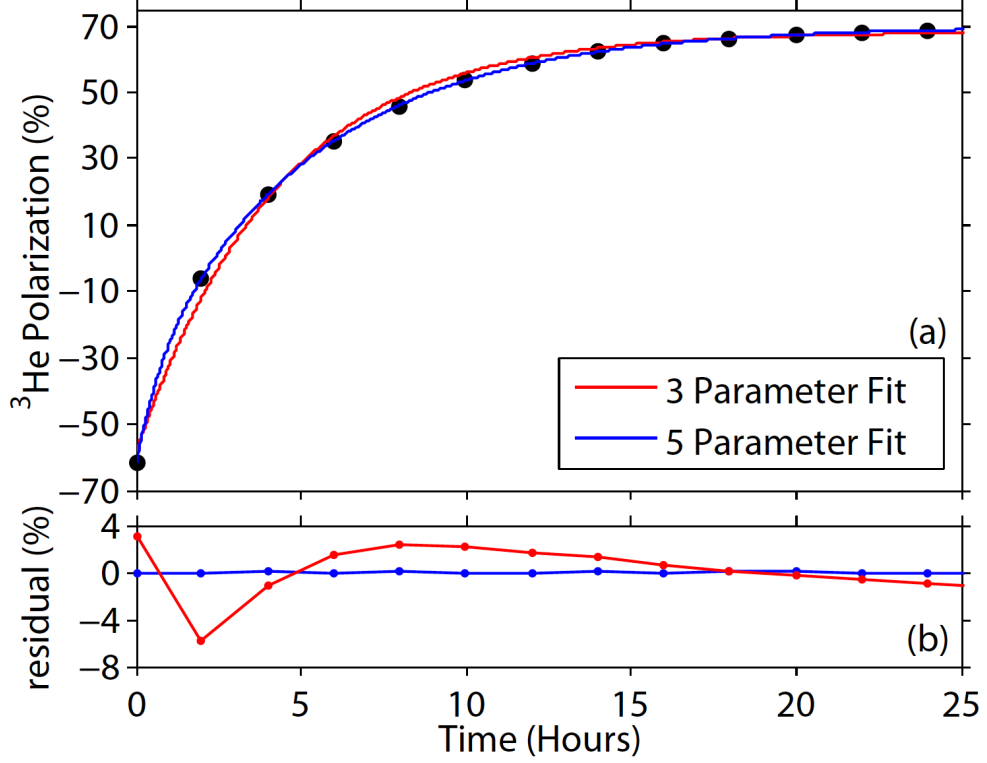
**Figure 3.3:** (a) Shown is a spinup of the target Brady. The spinup data has been fit with a 3-parameter and a 5-parameter formalism. (b) The residuals of the two fits. The error for 3-parameter fit is larger because it does not account for diffusion between two chambers.

The equation that describes spinups of single-chambered cell is:

$$P(t) = (P^0 - P^\infty)e^{-\Gamma_{sc}t} + P^\infty \tag{3.1}$$

where $P^\infty$ is the saturation polarization, $P^0$ is the initial polarization, $\Gamma_{sc} = \gamma_{se}(1 + X) + \Gamma$ is the spin up rate of the buildup of polarization. The subscript "sc" here stands for "single chamber" to differ from the spinup rate of double-chambered

cell. $\gamma_{se}$ is the spin-exchange rate, X is the X factor that limits the maximal achievable polarization, which will be discussed in more detail later in the chapter. $\Gamma$ is the spin relaxation rate. When using this equation to fit spinup, there are only three parameters, hence the name 3-parameter fit. The saturation polarization is given by:

$$P^\infty = \frac{\langle P_A \rangle \gamma_{se}}{\Gamma_{sc}} = \frac{\langle P_A \rangle \gamma_{se}}{\gamma_{se}(1+X)+\Gamma} \tag{3.2}$$

where $\langle P_A \rangle$ is the polarization of the alkali vapor averaged over the cell.

The following derivation will only focus on double-chambered cell. The polarization accumulation rate can be described by

$$\frac{dP_{pc}}{dt} = \Gamma_{se}(P_A - P_{pc}) - \Gamma_{pc}P_{pc} - d_{pc}(P_{pc} - P_{tc}) \tag{3.3a}$$

$$\frac{dP_{tc}}{dt} = -\Gamma_{tc}P_{tc} + d_{tc}(P_{pc} - P_{tc}) \tag{3.3b}$$

where $P_{pc}(P_{tc})$ is the $^3$He polarization in PC (TC); $\gamma_{se}$ is the spin-exchange rate in PC; $\Gamma_{pc}(\Gamma_{tc})$ is the relaxation rate o $^3$He polarization in PC (TC); $d_{pc}(d_{tc})$ is the probability for a nucleus to leave PC (TC) and enter TC (PC). The transfer rates $d_{pc}$ and $d_{tc}$ are related by:

$$f_{pc}d_{pc} = f_{tc}d_{tc} \tag{3.4}$$

where $f_{pc}(f_{tc})$ is the fraction of atoms in PC (TC). The solutions to Eq.3.3 are

$$P_{pc}(t) = C_{pc}e^{-\Gamma_f t} + (P^0_{pc} - P^\infty_{pc} - C_{pc})e^{-\Gamma_s t} + P^\infty_{pc} \tag{3.5a}$$

$$P_{tc}(t) = C_{tc}e^{-\Gamma_f t} + (P^0_{tc} - P^\infty_{tc} - C_{tc})e^{-\Gamma_s t} + P^\infty_{tc} \tag{3.5b}$$

where $P_{pc}^0(P_{tc}^0)$ is the initial polarization in the pumping (target) chamber, $P_{pc}^\infty(P_{tc}^\infty)$ is the saturation polarization in the pumping (target) chamber. The "slow" time constant $\Gamma_s$ is mostly determined by the volume averaged spin-exchange rate, which is given by

$$\Gamma_s = \langle\gamma_{se}\rangle(1+X) + \langle\Gamma\rangle - \delta\Gamma \tag{3.6}$$

where $\langle\gamma_{se}\rangle = f_{pc}\gamma_{se}$ is the cell averaged spin-exchange rate, $\langle\Gamma\rangle$ is the cell averaged spin relaxation rate, as the rate might be different for pumping chamber and target chamber. The quantity $\delta\Gamma$ contains corrections due to the finite speed at which polarization moves between the two chambers. The size of $\delta\Gamma$ is usually no more than 10% of the size of $\Gamma_s$ in our studies, and never more than 15%.

Detailed discussion is done by Dolph**??**. Again, the name 5-parameter fit comes from the fact that there are 5 parameters in each of the two equations. It's interesting to note the time evolution of $^3$He polarization for double-chambered cells has a new time constant: the "fast" time constant $\gamma_f$ that is dominated by the diffusion rates $d_{pc}$ and $d_{tc}$ when diffusion is relatively fast. In the fast-transfer limit, double-chambered solution reduces to single-chambered solution.

The other interesting point is the relation between the saturation polarization in PC and TC

$$P_{tc}^\infty = \frac{P_{pc}^\infty}{1 + \frac{\Gamma_{tc}}{d_{tc}}} \tag{3.7}$$

In the fast-transfer limit where $d_{tc} \gg \Gamma_{tc}$, $P_{tc}^\infty = P_{pc}^\infty$.
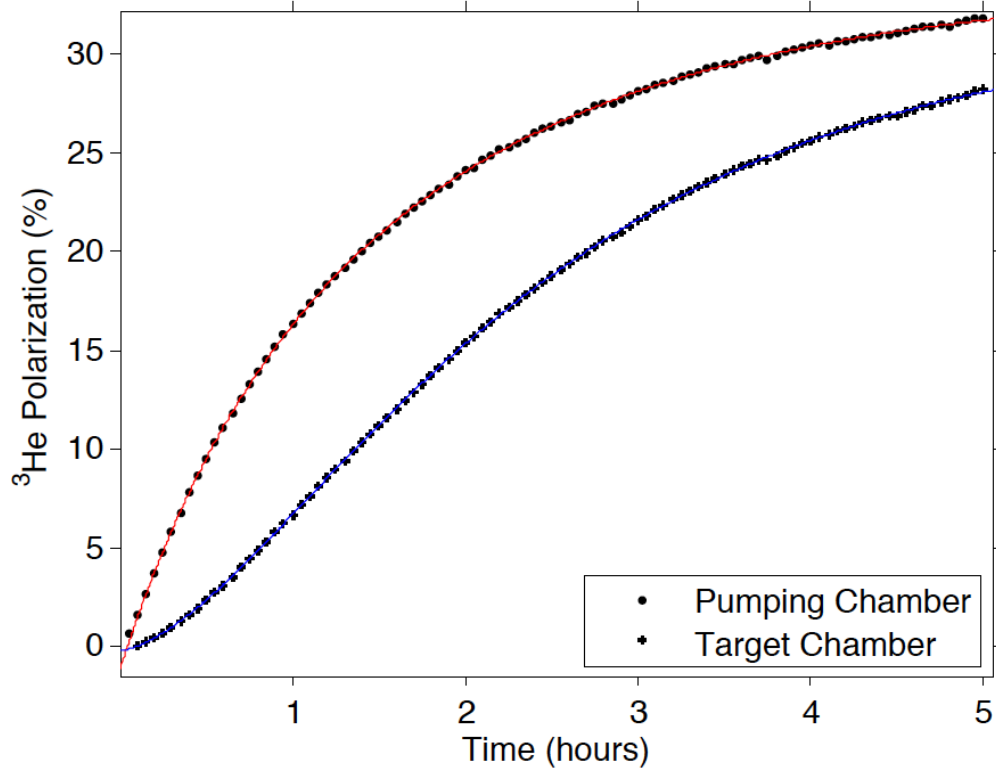
**Figure 3.4:** $^3$He polarization as a function of time for both the pumping chamber and the target chamber. The top curve is the pumping chamber and the bottom curve is the target chamber. Data was taken at a fast pace so there would be enough points to demonstrate the initial behavior.

### 3.2.1.3  Initial Spinup

As shown in Fig.3.4, the early behavior of spinup with zero polarization for the pumping chamber and the target chamber are quite different. The initial part of the pumping chamber is almost linear but the target chamber shows a curved initial part. By performing a Taylor expansion on Eq. 3.5 we obtain the initial part of the spinup for both chambers:

$$P_{pc}(t) = \gamma_{se} P_A t - \frac{1}{2}\gamma_{se} P_A (\gamma_{se} + \Gamma_{pc} + d_{pc})t^2 \qquad (3.8a)$$

$$P_{tc}(t) = \frac{1}{2}\gamma_{se} P_A d_{tc} t^2 \qquad (3.8b)$$

where $\gamma_{se}$ is the spin-exchange rate in the pumping chamber and $P_A$ is the alkali polarization. The dominant term in $P_{pc}(t)$ is the linear term while the shape of $P_{tc}(t)$ is quadratic.

The slope of the linear shape of initial spinup of the pumping chamber gives access to the product $P_A\gamma_{se}$ and fitting the initial spinup of the target chamber to a quadratic function provides the product $\gamma_{se}P_A d_{tc}$. The alkali polarization $P_A$ can be measured with a technique named Faraday rotation, we then gain knowledge of the spin-exchange rate $\gamma_{se}$ and the diffusion rate $d_{tc}$. The slope of the polarization buildup in the pumping chamber is often written as $m_{pc} = P_A\gamma_{se}$.

The spin relaxation rate is also of great importance for characterizing target cells. The relaxation rates in the pumping chamber and the target chamber are different due to geometric and other properties. The cell-average relaxation rate can then be written as

$$\langle\Gamma\rangle = f_{pc}\Gamma_{pc} + f_{tc}\Gamma_{tc} \qquad (3.9)$$

where $f_{pc}$ ($f_{tc}$) is the fraction of atoms in PC (TC); $\Gamma_{pc}$ ($\Gamma_{tc}$) is the average relaxation rate in PC (TC). When the cell is being pumped by laser, the pumping chamber is heated with hot air to create alkali vapor while the target chamber remains at the room temperature. Difference in temperature further complicates difference in relaxation rates between the two chambers. However, when trying to measure the

life time (the inverse of the relaxation rate) of the cell, we typically keep the entire cell at room temperature and perform a "spindown" measurement.

During a spindown, the cell starts with some polarization (normally as high as possible so we can obtain a more complete curve), and relaxes on its own while we take AFP measurements at a certain rate. Typically, the interval between measurements is anywhere between 30 mins and 2 hrs, depending on the lifetime of the cell. The rule of thumb is to take AFP frequently enough so the spindown curve has sufficient data points while not too often so the polarization relaxes too fast due to AFP losses. The $^3$He polarization relaxation can be described by

$$P(t) = P_0 e^{-t/\tau_{true}} \tag{3.10}$$

The true lifetime $\tau_{true}$ of the cell without relaxation due to AFP loss can be measured with two methods: the first is to take 5 AFP measurements consecutively with very short interval (normally around 3 minutes), the second is to perform several spindown measurements, each with a different interval.

In the first method, because the lifetime of the cell is much longer than 3 minutes, we can safely attribute all losses to AFP measurements and extract the loss due to a single AFP $loss_{afp}$. The data values can then be corrected with the equation

$$S_i^{corrected} = S_i^{raw}/(1 - loss_{afp})^{i-1} \tag{3.11}$$

where $S_i^{corrected}$ is the corrected signal, $S_i^{raw}$ is the raw signal, i represents it is the $i$th measurement in the spindown, $loss_{afp}$ is the loss due to a single measurement. Fitting the corrected values to Eq. 3.10 gives the true lifetime $\tau_{true}$.

A simple example for the second method would be to perform one spindown with one-hour interval and another spindown with two-hour interval, the relaxation rates in these two spindowns are

$$\frac{1}{\tau_{1hr}} = \frac{1}{\tau_{true}} + \Gamma_{AFP\_1hr} \tag{3.12a}$$

$$\frac{1}{\tau_{2hr}} = \frac{1}{\tau_{true}} + \Gamma_{AFP\_2hr} \tag{3.12b}$$

$$\Gamma_{AFP\_1hr} = 2 \times \Gamma_{AFP\_2hr} \tag{3.12c}$$

where $\tau_{1hr}$ and $\tau_{2hr}$ are the lifetimes measured with taking AFP every 1 hour and every 2 hours, $\tau_{true}$ is the true lifetime of the cell without interference from measurements, $\Gamma_{AFP\_1hr}$ ($\Gamma_{AFP\_2hr}$)is the relaxation rate due to taking measurements every 1hr (2hr). We can then solve for $\tau_{true}$.

## 3.3 The K-$^3$He Spin-Exchange Rate Constant

As mentioned in the initial spinup section, the polarization in the pumping chamber at the beginning of accumulation process if started with completely unpolarized state can be described by

$$P_{pc} = \gamma_{se}\langle P_A \rangle (t - t_0) + b(t - t_0)^2 = m_{pc}t + bt^2 + c \tag{3.13}$$

where $m_{pc}$ is the slope of the linear term. Typically, in the first 20 to 30 minutes, the spinup behaves so linearly that the effect of quadratic term is negligible.

During these initial spinups, an AFP measurement was taken every 3 minutes. The AFP losses were carefully accounted for when calculating $m_{pc}$. The $^3$He spins

were flipped to the opposite direction during every AFP measurement for a short period of time while still receiving polarization in the original direction. Care was taken to account for the time during which spins were "anti-aligned". We refer to the the slope collected from initial spinups as $m_{pc}^s$, to differentiate it from the same quantity measured with the Faraday rotation technique. I will briefly introduce Faraday rotation, the details were described thoroughly by Dolph. [?].

The Faraday rotation technique, as the name implies, is the observation of Faraday rotation using a linearly polarized probe laser. Faraday rotation refers to the change in the orientation of the polarization axis when linearly polarized light passes through a polarized alkali vapor. It is sufficient to consider only the alkali-metal atom's $D_1$ and $D_2$ lines for our case, the Faraday rotation angle $\phi_r$ is:

$$\phi_r(\nu) = \left(\frac{r_e c}{6}\right) P_A cos(\theta)[Rb]l\{F_{Rb}(\nu) + DF_K(\nu)\} \tag{3.14}$$

where $r_e$ is the classical electron radius, c is the speed of light in vacuum, l is the path length through the vapor, D is the ratio of the K to Rb vapor number densities, $F_A(\nu)$ is the frequency dependence of alkali species A.

During a Faraday rotation measurement, $\phi_r$ was measured at several probe wavelengths and fit to the Eq. 3.14. We were able to obtain the quantities $P_A[Rb]l$ and D from the fit. However, in order ot extract [Rb], it is necessary to measure the path length l and $P_A$. Alkali polarization was measured by measuring the Faraday rotation angle while inducing Zeeman transition. It is worth noting this only gave line-averaged polarization as only information on the path of the probe laser was collected. The volume-averaged alkali polarization can be obtained by applying small

corrections from our simulation.

With knowledge of alkali densities, the spin-exchange rate is:

$$\gamma_{se} = k_{se}^{Rb}[Rb] + k_{se}^{K}[K] \tag{3.15}$$

where $k_{se}^{Rb}(k_{se}^{K})$ is the spin-exchange rate constant between $^3$He and Rb (K). The $m_{pc}$ calculated with this manner is referred as $m_{pc}^{F}$, since this quantity was computed with Faraday rotation data.

The values of $m_{pc}^{F}$ and $m_{pc}^{s}$ are expected to be the same if they are measured against the same cell under identical conditions. The spin-exchange rate constants $k_{se}^{Rb}$ and $k_{se}^{K}$ are required to calculate $m_{pc}^{F}$. $k_{se}^{Rb}$ has been measured and reported in literature multiple times. $k_{se}^{K}$ on the other hand, is not as well-known. The value of $k_{se}^{Rb}$ we used was the combined result from Baranga *et al.* [?] and from Chann *et al.* [?]:

$$k_{se}^{Rb} = (6.79 \pm 0.14) \times 10^{-20} cm^3/s \tag{3.16}$$

The ratio of $m_{pc}^{F}/m_{pc}^{s}$ is plotted in Fig. **??**. The two measurements with the Rb only cell Sosa are shown with solid circles. To calculate the ratio for the rest of the measurements, a value for $k_{se}^{K}$ is needed. Babcock reported this number to be $(5.5 \pm 0.4) \times 10^{-20} cm^3/s$ in his thesis. However, the resulting ratio was significantly lower than unity in all but one of the 6 measurements, as shown with open diamonds in the figure. We fit our data so the ratio $m_{pc}^{F}/m_{pc}^{s}$ is equal to one while treating $k_{se}^{K}$ as a free parameter. The results are shown with solid diamonds. Our fitted $k_{se}^{K}$ value is
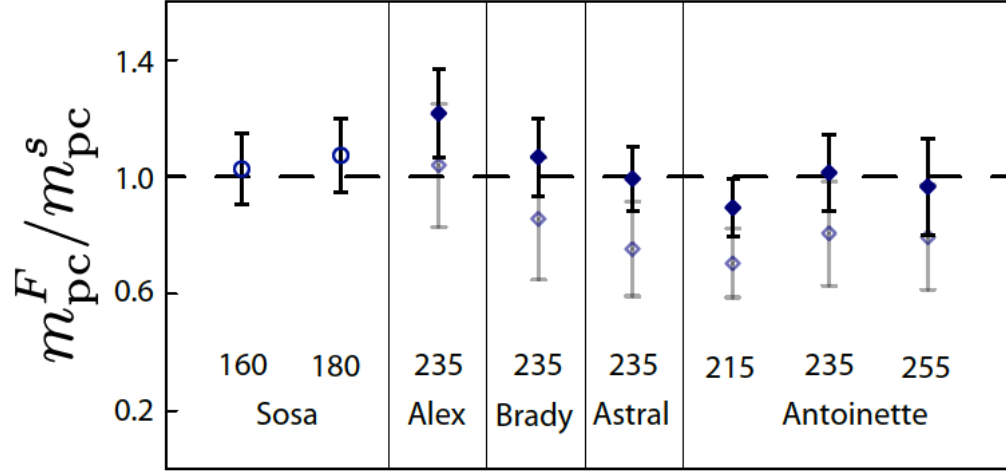
**Figure 3.5:** Plotted is the ratio $\mathrm{m}_{pc}^{F}/\mathrm{m}_{pc}^{s}$ for eight separate measurements. The numbers above the cell names are the oven set temperatures at which the measurements were made.

$$k_{se}^{K} = (7.46 \pm 0.62) \times 10^{-20} cm^{3}/s \tag{3.17}$$

The reason why our result is significantly higher than Babcock's is unclear. One possibility may be temperature dependence as the temperatures under which our measurements were made were higher than that of Babcock's. We decided to use our own result of $k_{se}^{K}$ to measure the X factor because it was measured under similar operating conditions to our other measurements, and our own result improves internal consistency of our data.

## 3.4  The X Factor

Prior to the introduction of the X factor, it was believed that $^3$He polarization could approach unity with sufficiently high alkali vapor densities and laser power such that $P_A$ is nearly 100% and $\gamma_{se} \gg \langle \Gamma \rangle$. However, the $^3$He polarization during our studies had shown differently. The fact that it was never close to 100% even with high laser power and alkali densities could be explained by the X factor.

As mentioned earlier, Babcock *et al.* reported a previously unrecognized spin relaxation mechanism in his paper [**?**]. This mechanism appears to be roughly proportional to the spin-exchange rate $\gamma_{se}$, so it cannot be overcome by increasing the alkali density or laser power. The maximal achievable $^3$He polarization can be expressed as

$$\lim_{\gamma_{se} \to \infty} = \lim_{\gamma_{se} \to \infty} \frac{\langle P_A \rangle \langle \gamma_{se} \rangle}{\langle \gamma_{se} \rangle (1 + X) + \langle \Gamma \rangle} = \frac{P_A}{1 + X} \tag{3.18}$$

The combination of alkali-hybrid and narrowband laser has made it much easier to achieve higher spin-exchange rates $\gamma_{se}$. Thus X factor is playing an increasingly more significant role in limiting the equilibrium $^3$He polarization, which makes it an important subject ot study.

Unlike many other properties of the cell that could be measured directly, X factor is a derived quantity. While characterizing our target cells, we collected enough data to determine X factor in several different ways. We were able to compare these values and combine them into weighted averages. We also looked at possible temperature dependence using X values obtained at different temperatures. The data used is presented in Table 3.2.

| EXP | Cell | Lasers | $I_0$ W/cm² | $T_{pc}^{set}$ °C | $P_{He}^\infty$ | $\Gamma_s^{-1}$ hrs | $\langle\Gamma\rangle^{-1}$ hrs | $\langle P^A\rangle$ | $P_{line}^A$ | $D_{fr}$ | $D_{pb}$ | $[Rb]_{fr}$ $10^{14}$/cm³ | $\Delta T_{Rb}$ °C | $\Delta T_{He}$ °C | X |
|---|---|---|---|---|---|---|---|---|---|---|---|---|---|---|---|
| saGDH | Proteus | 3B | 3.8 | 180 | 0.46 | 27 | 74 | - | - | 0 | 0 | - | - | - | - |
| | Priapus | 3B | 3.8 | 180 | 0.44 | 21 | 56 | - | - | 0 | 0 | - | - | - | - |
| | Penelope | 3B | 3.8 | 180 | 0.39 | 18 | 46 | - | - | 0 | 0 | - | - | - | - |
| | Powell | 3B | 3.8 | 180 | 0.38 | 13 | 25 | - | - | 0 | 0 | - | - | - | - |
| | Prasch | 3B | 3.8 | 180 | 0.33 | 13 | 33 | - | - | 0 | 0 | - | - | - | - |
| GEN | Al | 2.5B | 3.2 | 235 | 0.53(03) | 7.86(05) | 27.42(1.37) | - | - | - | 4.53(25) | - | - | - | - |
| | Al | 5B | 6.1 | 235 | 0.54(03) | 6.73(18) | 27.42(1.37) | - | - | - | 4.53(25) | - | - | - | - |
| | Barbara | 2.5B | 1.6 | 235 | 0.37(02) | 5.5(08) | 42.95(2.15) | - | - | - | 4.80(25) | - | - | - | - |
| | Barbara | 5B | 3.1 | 235 | 0.57(03) | 4.76(63) | 42.95(2.15) | - | - | - | 4.80(25) | - | - | - | - |
| | Gloria | 3B | 1.7 | 235 | 0.60(03) | 6.13(04) | 38.29(1.91) | - | - | - | 7.20(40) | - | - | - | - |
| | Anna | 1B | 0.6 | 235 | 0.33(02) | 5.60(34) | 11.38(57) | - | - | - | 9.64(57) | - | - | - | - |
| | Anna | 1.5B | 1.0 | 235 | 0.39(02) | 5.37(08) | 11.38(57) | - | - | - | 9.64(57) | - | - | - | - |
| | Dexter | 1.5B | 1.5 | 235 | 0.47(02) | 7.58(17) | 18.45(92) | - | - | - | - | - | - | - | - |
| | Dexter | 5B | 6.1 | 235 | 0.49(02) | 6.63(12) | 18.45(92) | - | - | - | - | - | - | - | - |
| | Edna | 3B | 2.4 | 235 | 0.56(03) | 5.71(02) | 27.42(1.37) | - | - | - | 3.63(20) | - | - | - | - |
| | Dolly | 3B | 1.0 | 235 | 0.43(02) | 6.16(03) | 35.24(1.76) | - | - | - | 20(1.3) | - | - | - | - |
| | Dolly | 1N1B | 1.4 | 235 | 0.62(03) | 5.79(07) | 35.24(1.76) | - | - | - | 20(1.3) | - | - | 17(10) | - |
| | Simone | 2N1B | 3.8 | 215 | 0.31(01) | 14.08(06) | 22.87(1.14) | 0.947(020) | 0.91(05) | 10.66(54) | 8.89(45) | 0.20(02) | -7(3) | - | -0.04(12)* |
| | Simone | 2N1B | 3.8 | 240 | 0.48(02) | 6.89(20) | 22.87(1.14) | - | - | - | 9.76(49) | - | - | - | - |
| | Simone | 2N1B | 3.8 | 255 | 0.58(02) | 6.45(10) | 22.98(1.14) | 0.929(023) | 0.92(05) | 12.48(83) | 10.3(52) | 0.90(09) | -4(5) | - | 0.11(06)* |
| | Sosa | 2N1B | 1.9 | 160 | 0.57(02) | 16.69(09) | 73.68(3.68) | 0.966(020) | 1.00(03) | 0 | 0 | 1.97(13) | 4(1) | 30(7) | 0.24(06)† |
| | Sosa | 2N1B | 1.9 | 170 | 0.61(03) | 11.67(04) | 73.68(3.68) | 0.964(020) | 0.98(03) | 0 | 0 | 3.00(33) | 3(3) | 38(14) | 0.27(06)* |
| | Sosa | 2N1B | 1.9 | 180 | 0.55(02) | 8.79(09) | 73.68(3.68) | 0.954(022) | 0.97(03) | 0 | 0 | 4.30(27) | 1(2) | 47(7) | 0.43(06)† |
| | Sosa | 2N1B | 1.9 | 190 | 0.40(02) | 6.39(22) | 73.68(3.68) | 0.854(075) | 0.82(03) | 0 | 0 | 5.69(63) | -2(3) | 48(20) | 0.58(12)* |
| | Sosa | 2N1B | 1.9 | 200 | 0.26(01) | 5.04(17) | 73.68(3.68) | - | - | 0 | 0 | - | - | 43(18) | - |
| Transversity | Boris | 3B | 1.8 | 235 | 0.42(02) | 6.25(04) | 23.74(1.19) | 0.871(050) | 0.79(07) | 1.96(18) | 2.45(23) | 2.19(34) | -8(7) | - | 0.26(10)* |
| | Samantha | 3B | 1.8 | 235 | 0.50(02) | 6.30(13) | 36.51(1.83) | - | - | - | 4.34(23) | - | - | - | - |
| | Samantha | 3N | 2.6 | 235 | 0.68(03) | 4.62(03) | 22.13(1.11) | 0.956(020) | 0.99(03) | 4.37(10) | 4.34(23) | 1.80(10) | 7(2) | 21(10) | 0.12(05)* |
| | Alex | 2N1B | 2.6 | 235 | 0.59(03) | 4.81(02) | 32.96(1.65) | 0.942(042) | 0.99(03) | 1.37(08) | 1.19(07) | 4.08(36) | 0(4) | 42(10) | 0.34(06)† |
| | Moss | 1N1B | 1.8 | 235 | 0.62(03) | 5.35(04) | 33.00(1.65) | - | 0.95(09) | - | 2.40(13) | - | - | 29(8) | - |
| | Tigger | 1N1B | 1.8 | 235 | 0.51(02) | 4.89(05) | 12.62(63) | - | 0.95(09) | - | - | - | - | 23(9) | - |
| | Astral | 2N1B | 2.6 | 235 | 0.69(03) | 6.57(12) | 48.90(2.45) | 0.954(020) | 0.99(03) | 7.09(55) | 6.21(56) | 0.97(09) | 3(5) | 25(4) | 0.17(05)† |
| | Stephanie | 3N | 2.6 | 235 | 0.63(03) | 4.55(09) | 48.35(2.42) | 0.929(114) | 0.99(03) | 1.39(11) | 1.50(10) | 5.08(58) | 7(5) | 54(6) | 0.31(08)* |
| | Brady | 1N | 0.9 | 235 | 0.62(03) | 4.82(1.08) | 33.50(1.68) | - | 0.95(03) | - | 2.36(24) | - | - | 14(9) | - |
| | Brady | 2N | 1.8 | 235 | 0.68(03) | 5.52(70) | 33.50(1.68) | - | 0.99(03) | - | 2.36(24) | - | - | 25(8) | - |
| | Brady | 3N | 2.6 | 235 | 0.70(03) | 5.30(01) | 33.50(1.68) | 0.956(021) | 0.99(03) | 2.60(20) | 2.36(24) | 2.86(30) | 6(5) | 39(9) | 0.14(05)† |
| | Maureen | 3N | 2.6 | 235 | 0.66(03) | 5.42(12) | 29.21(1.46) | - | 0.97(09) | - | 4.42(55) | - | - | 32(12) | - |
| | Antoinette | 3N | 1.7 | 215 | 0.49(02) | 6.63(37) | 20.93(1.05) | 0.958(020) | 0.99(03) | 2.85(13) | - | 0.96(07) | 0(3) | 16(8) | 0.28(08)† |
| | Antoinette | 3N | 1.7 | 235 | 0.61(03) | 4.18(10) | 20.93(1.05) | 0.936(043) | 0.99(03) | 3.32(27) | - | 1.83(20) | 0(5) | 20(10) | 0.24(07)† |
| | Antoinette | 3N | 1.7 | 255 | 0.41(02) | 2.66(11) | 20.93(1.05) | 0.776(099) | 0.93(10) | 3.57(23) | - | 2.88(39) | -5(6) | 33(9) | 0.55(13)† |

**Table 3.2:** Cell Performance for three sets of experiments: saGDH (top), GEN (middle), and Transversity & $d_2^n$ (bottom). Within each experiment grouping, data is grouped by type of laser used (B = Broadband, N = Narrowband). $I_0$ is the nominal incident laser intensity at the center of the pumping chamber. $T_{pc}^{set}$ is the oven set temperature. $P_{pc}^\infty$ is the equilibrium polarization in the pumping chamber and $\Gamma_s$ is the slow time constant extracted from the five parameter fit to the polarization build up curve. $\Gamma_c$ is the cell-averaged room temperature spin relaxation rate. $\langle P_A\rangle/P_A^l$ is the volume averaged to line averaged alkali polarizaiton ratio determined from the optical pumping simulation. $P_A^l$ is the measured line averaged alkali polarization. $D_{fr}\&D_{pb}$ are the K to Rb density ratios determined from Faraday rotation and pressure broadening measurements. $[Rb]_{fr}$ is the Rb number density measured from Faraday rotation. $\Delta T_{He}$ is the temperature of Rb inferred from the number density relative to the oven set temperature. $\Delta T_{He}$ is the temperature of $^3$He inferred from temperature tests relative to the oven set temperature. X is the best combined value for the X-factor. * indicates X was measured using only spinup, alkali polarization, and Faraday rotation data. † indicates X was also measured using the early-time behavior of the spinup.

We calculated the X factors in several different ways, all of which required knowledge of the cell-averaged spin relaxation rate $\langle\Gamma\rangle$ at operating temperatures. However, the spindown measurements we performed only gave us the spin relaxation rate $\langle\Gamma\rangle_c$ at room temperature. We made the assumption that the difference between $\langle\Gamma\rangle$ and $\langle\Gamma\rangle_c$ is purely due to the change of cell-averaged $^3$He-$^3$He dipolar spin relaxation rate, and the relaxation rate due to collisions with the walls is the same for the two chambers and does not change at different temperature. The correction to the relaxation rate is given by

$$\langle\Gamma\rangle = \langle\Gamma\rangle_c - [n_0 - f_{pc}n_{pc}/f^d(t_{pc}) - f_{tc}n_{tc}/f^d(t_{tc})]/\tau^d \tag{3.19}$$

where $n_0$ is the $^3$He fill density, $n_{pc(tc)}$ is the $^3$He density in the pumping (target) chamber, $f_{pc(tc)}$ is the fraction of $^3$He atoms in the pumping (target) chamber, $t_{pc} = T_{pc}/(296.15K)$, $t_{tc} = (313.15K)/(296.15K)$, $\tau^d = 744 hrs \cdot amg$, $f^d(t)$ is a function that parameterizes the temperature dependence of the dipolar relaxation [?]. $\langle\Gamma\rangle$ for is typically only a few percent less than $\langle\Gamma\rangle_c$ for us. In addition, whenever the quantity $(\Gamma_s - \langle\Gamma\rangle)$ is used, a small correction to account for the AFP losses is added.

Our methods of extracting X require using some form of the equation

$$\langle\gamma_{se}\rangle = \frac{\Gamma_s - \langle\Gamma\rangle + \delta\Gamma}{1 + X} \tag{3.20}$$

One method Babcock used and we applied on a small number of cells is called "hot relaxation method". We plot $\langle\gamma_{se}\rangle$ as a function of $\Gamma_s - \langle\Gamma\rangle + \delta\Gamma$, the slope of a linear fit to the data is expected to be 1/(1+X). Three such fits are shown in Fig. ??, all of which were constrained to go through the origin. Two of the three X

values were significantly different than zero. The X factor of Simone is too close to zero when taken the error into account for us to make a strong statement.

The small correction $\delta\Gamma$ came into play because of the double-chambered design. It can be approximated by

$$\delta\Gamma \approx f_{pc}f_{tc}(d_{pc} + d_{tc})u^2 + higher\ order\ terms \tag{3.21}$$

where $d_{pc(tc)}$ is the probability per unit time that a $^3$He atom will exit the pumping (target) chamber. The quantity u is

$$u = \frac{\gamma_{se}(1 + X) + \Gamma_{pc} - \Gamma_{tc}}{d_{pc} + d_{tc}} \tag{3.22}$$

where $\Gamma_{pc(tc)}$ is the spin relaxation rate in the pumping (target) chamber. What makes the determination of X tricky is that we need to know its value before we can calculate u which is a prerequisite for X. However, because $\delta\Gamma$ is such a small correction typically being 10% of less of the size of $\Gamma_s$, we solve this problem in an iterative manner. X is initially assumed to be 0 and plugged into Eq. 3.22, which in the end lead to a different value of X that is closer to its real value. After iterating this process a few times, X quickly converges to a stable value.

However, the hot relaxation method assumes the temperature dependence of the X factor is identical to the temperature dependence of $\gamma_{se}$ by combining data taken at different temperature into one value of X. It is also time consuming to perform measurements shown in Fig. **??**. For these two reasons, the hot relaxation method was only applied to a small number of cells.

In order to measure X factor at a single temperature and explore its temperature
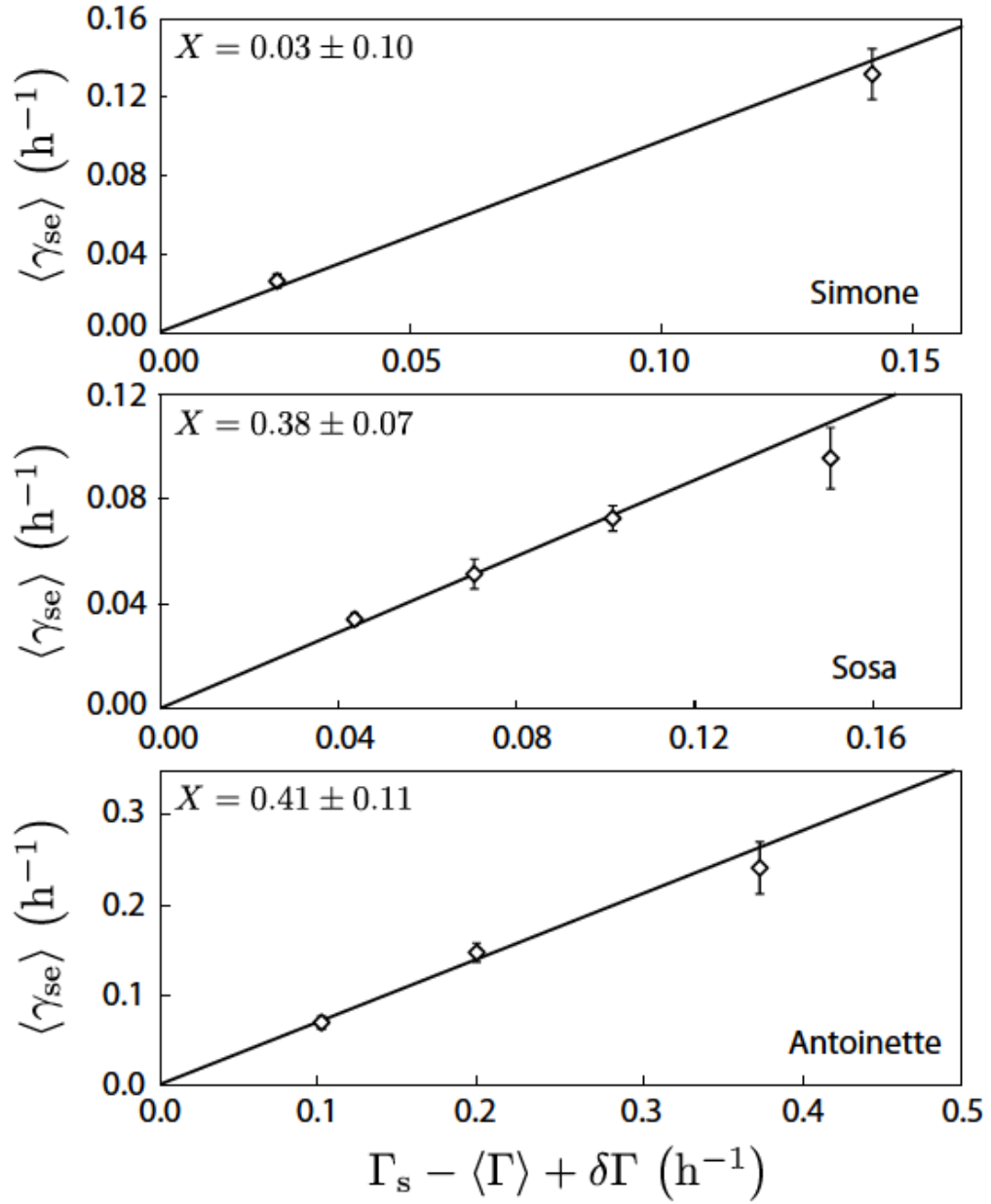
**Figure 3.6:** The cell-averaged spin-exchange rate $\langle \gamma_{se} \rangle$ is calculated using data from Faraday rotation and the spin-exchange constants $k_{se}^{Rb}$ and $k_{se}^{K}$. The three linear fits shown here are constrained to go through zero. The errors quoted in values of X factor include the uncertainty in our determination of $k_{se}^{K}$.

dependence, we used 4 four other methods to determine the value of X factor. All but the second method described below are based on the "polarization method" from Ref. [?]. The difference is that we used early time measurements of the initial spinups for $P_A \langle \gamma_{se} \rangle$ for the third and fourth methods. And the second method is basically a single point measurement of the hot relaxation method described above.

We label the results from the four single temperature methods as $X_1$, $X_2$, $X_3$ and $X_4$ respectively. The most straightforward method requires measurements of $\langle P_A \rangle$, $P_{pc}^\infty$ and $\Gamma_s$. The equilibrium $^3$He polarization can be rewritten as

$$P_{pc}^\infty = \frac{\langle P_A \rangle \langle \gamma_{se} \rangle}{\Gamma_s + \delta\Gamma - \delta\Gamma'} \tag{3.23}$$

where $\delta\Gamma' = f_{tc}\Gamma_{tc}^2/(\Gamma_{tc} + d_{tc})$. Substitute Eq. 3.20 into Eq. 3.23, $X_1$ is

$$X_1 = \frac{\langle P_A \rangle}{P_{pc}^\infty} \left( \frac{\Gamma_s - \langle \Gamma \rangle + \delta\Gamma}{\Gamma_s + \delta\Gamma - \delta\Gamma'} \right) - 1 \tag{3.24}$$

Just as what we did for the hot relaxation method, here $\delta\Gamma$ is calculated in the same iterative manner. X is first taken as 0 and the iteration continued until X converged to a stable value.

For the second method, we first solve Eq. 3.20 for X:

$$X = \frac{\Gamma_s - \langle \Gamma \rangle + \delta\Gamma}{\langle \gamma_{se} \rangle} - 1 \tag{3.25}$$

then we substitute Eq. 3.15 into the equation above:

$$X_2 = \frac{\Gamma_s - \langle \Gamma \rangle + \delta\Gamma}{f_{pc}k_{se}^{Rb}[Rb](1 + D')} - 1 \tag{3.26}$$

Again $\delta\Gamma$ is calculated iteratively. We chose to use our value of $k_{se}^K$ for better consistency with the rest of our data.

The third method is very similar to the second, but we determine $\langle\gamma_{se}\rangle$ with data from initial spinups:

$$\langle\gamma_{se}\rangle = f_{pc}m_{pc}^s/\langle P_A\rangle \tag{3.27}$$

Substitute the above equation into Eq. 3.25, we get

$$X_3 = \langle P_A\rangle\frac{\Gamma_s - \langle\Gamma\rangle + \delta\Gamma}{f_{pc}m_{pc}^s} - 1 \tag{3.28}$$

Note the quantity $k_{se}^K$ used for $X_2$ was obtained by fitting the ratio $m_{pc}^F/m_{pc}^s$ to 1, thus for any hybrid cell, $X_2$ and $X_3$ are highly correlated. However, for pure Rb cell such as Sosa, these two methods are independent.

The fourth method is similar to the first one. It starts from Eq. 3.23, what makes it different from the first method is that it treats $\langle\gamma_{se}\rangle$ as a known quantity and expresses $\Gamma_s$ with it using Eq. 3.20, while the first method did it in the exact opposite way. Then the cell-averaged spin-exchange rate is evaluated with

$$\langle\gamma_{se}\rangle = f_{pc}m_{pc}^s/\langle P_A\rangle \tag{3.29}$$

Thus $X_4$ is

$$X_4 = \frac{P_A}{P_{pc}^\infty} - \frac{\langle P_A\rangle(\langle\Gamma\rangle - \delta\Gamma')}{f_{pc}m_{pc}^s} - 1 \tag{3.30}$$

The computed X factors are shown in Table 3.3. The different values of X are quite consistent with each other. It is worth noting that even though $X_1$ is completely

75

| Cell | T(°C) | $X_1$ | $X_2$ | $X_3$ | $X_4$ | $X_{12}/X_{1234}$ |
|---|---|---|---|---|---|---|
| Simone | 215 | -0.02(12) | -0.10(14) | - | - | -0.04(12) |
| | 255 | 0.13(08) | 0.08(09) | - | - | 0.11(06) |
| Sosa | 160 | 0.22(07) | 0.28(09) | 0.32(15) | 0.18(09) | 0.24(06)$^{\dagger}$ |
| | 170 | 0.24(07) | 0.37(15) | - | - | 0.27(06) |
| | 180 | 0.45(08) | 0.40(09) | 0.50(17) | 0.45(09) | 0.43(06)$^{\dagger}$ |
| | 190 | 0.59(16) | 0.57(17) | - | - | 0.58(12) |
| Boris | 235 | 0.21(14) | 0.31(14) | - | - | 0.26(10) |
| Sam. | 235 | 0.08(06) | 0.22(09) | - | - | 0.12(05) |
| Alex | 235 | 0.34(09) | 0.35(09) | 0.63(20) | 0.29(10) | 0.34(06)$^{\dagger}$ |
| Astral | 235 | 0.15(07) | 0.22(10) | 0.20(14) | 0.14(07) | 0.17(05)$^{\dagger}$ |
| Steph. | 235 | 0.31(17) | 0.31(10) | - | - | 0.31(08) |
| Brady | 235 | 0.13(07) | 0.15(09) | 0.23(14) | 0.11(07) | 0.14(05)$^{\dagger}$ |
| Antoinette | 215 | 0.27(09) | 0.44(17) | 0.30(19) | 0.25(11) | 0.28(08)$^{\dagger}$ |
| | 235 | 0.20(09) | 0.34(12) | 0.36(17) | 0.15(09) | 0.24(07)$^{\dagger}$ |
| | 255 | 0.55(26) | 0.54(16) | 0.50(30) | 0.56(26) | 0.55(13)$^{\dagger}$ |

**Table 3.3:** Shown are the values of the X factor at the indicated over set temperatures. The last column is a weighted average of results from either the first two methods or all four methods. A $^{\dagger}$ indicates combined values computed with all 4 methods.

independent of $m_{pc}$ and $k_{se}^{K}$, it is still quite consistent with the rest of the X values. The last column in the table is a weighted average of either $X_1$ and $X_2$ ($X_{12}$) or all four X values ($X_{1234}$).

To the best of our knowledge, there has not been a dedicated study of the X factors and the their temperature dependence, with a large number of cells using measurements of the alkali polarization since the Babcock's *et al.* original work. Our results are an independent evidence of the existence of the X factor. According to our study, the X factor limits $^3$He polarization to 62-88% for the range of temperature we operate within.

Since we have evaluated X at multiple temperatures for Simone, Sosa and Antoinette, we can explore the temperature dependence of X factor. The combined value of X is plotted against temperature in Fig. **??** for the three cells. The figure seems to indicate a systematic variation with temperature.

If we assume a linear dependence of X with temperature, the fitted slope for Sosa with 4 points is $(0.012 \pm 0.002)/^{\circ}C$, which is six-sigma away from zero. The slope for the three points of Antoinette is $(0.007 \pm 0.005)/^{\circ}C$, which is slightly above one sigma from zero. Simone has only two points available to us, the second point seems to be right around the edge of the error bar on the first point. Although we cannot make a strong statement, but it is still likely that there is also a trend here. We do not consider this result conclusive, but they still suggest the existence of temperature dependence of X.

We considered the possibility that the temperature dependence was introduced by our own value of the spin-exchange constant $k_{se}^{K}$. After considering both our value and that from Babcock, we found that the trend exists with both, but our value provides
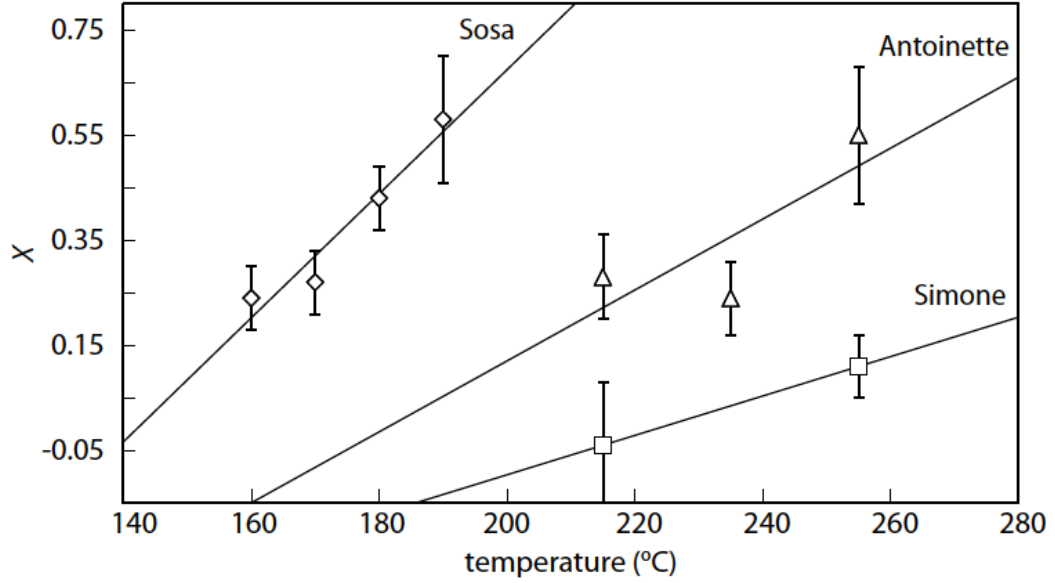
**Figure 3.7:** Shown are the combined values for X factor (either $X_{12}$ or $X_{1234}$ depending on the availability of data) versus temperature for the cell Sosa, Simone and Antoinette.

better self consistent. Another possibility is that the temperature dependence of $k_{se}^K$ is the source of temperature dependence of X. However, if that is the case, we should be able to observe different behaviors in what the 4 different methods produced. From what is shown by Table 3.3, the different methods produced similar results within errors, thus $k_{se}^K$ is not likely to be the cause of temperature dependence of X.

We also considered whether other systematic effects could result in such temperature dependence. For example, the distribution of the gas between pumping chamber and target chamber changes at different temperatures. We then concluded that the uncertainties in the gas distribution had only negligible effects on the observed temperature dependence of X. After analyzing our data, we were unable to identify a systematic effect as a plausible explanation, our results suggest further study of X

and its temperature dependence may be of great importance.

# Chapter 4

# Development of Hybrid Targets

## 4.1 Overview

Electron scattering experiments at JLab have traditionally used $^3$He targets made of glass due to the compatibility with spin-exchange optical pumping, the capability to be shape into desired geometries through glass blowing, and the excellent nuclear spin relaxation properties. The borosilicate glass Pyrex had been the glass of choice prior to the discovery that the much less permeable aluminosilicate glass generally provides longer spin-relaxation time. The most recent targets were thus composed entirely of the aluminosilicate glass GE180.

After the 12 GeV upgrade, JLab plans to run experiments with much higher electron beam currents. The maximum current used before the upgrade was $15\mu$A, while future experiments will be run at up to $60\mu$A. We believe an all-glass target cell might survive long enough for an experiment with $30\mu$A, but it is unlikely to survive at $60\mu$A. A natural solution would be to replace the thin glass window (where

electron beam enters and exits the target cell) with a material with higher strength and good spin-relaxation properties.

Deninger *et al.* from the Mainz group showed relaxation time of various metal surfaces: Mg (6 h), Al (6 h), Zn(12 h) etc. Gold caught our attention in particular, because it has a relatively long relaxation time of 20 h. This relaxation time was measured by coating the glass surface with gold, thus the area of gold surface was much larger than what will be needed for target windows. In addition, while the coating process made sure of the chemical purity, it did not make effort in ensuring the microscopic smoothness, which means the surface area was further increased. In light of this, our group have tested 19 cells with various geometries and materials, most of which incorporate a OFHC (Oxygen-free high thermal conductivity) copper tube with gold coating. OFHC copper was chosen as the substrate in most cases because of its structural strengths and the familiarity with manufacturers. Towards the end of my work, we achieved a 15.6 h relaxation time with a Pyrex cell that had a 5" long by 1" gold coated copper tube attached horizontally. By extrapolating the relaxation rate due to gold surface from this result, we believe the relaxation rate introduced by small metal windows in a target cell will be less than $1/135$ h$^{-1}$.

## 4.2 Wall Relaxation of $^3$He

### 4.2.1 Relaxation on Glass Surfaces

Fitzsimmons and Walters have studied surface-induce spin-lattice relaxation times as a function of temperature for $^3$He gas in glass containers [**?**]. There are mainly two

categories of wall relaxation mechanisms: ${}^3$He adsorption on the glass surface and the permeation of ${}^3$He into glass. The latter mechanism can be greatly reduced by using impermeable aluminosilicate glass such as GE180.

Timsit and Daniels [?] then studied surface relaxation on a great number of common materials and presented a phenomenological model to describe the relaxation processes.For permeable glasses, the relaxation is determined by absorption of gas in the surface layer of the glass and by the paramagnetic impurity content of the glass. The surface adsorption of ${}^3$He near paramagnetic sites on the walls also contributes to the nuclear relaxation. Relaxation due to absorption for permeable glasses will be discussed first below.

The diffusion coefficient $D$ of a noble gas in a glass can be calculated with the following equation:

$$D = D_0 e^{-Q_d/kT} \tag{4.1}$$

where $Q_d$ is the activation energy for diffusion and $D_0$ is a constant. The diffusion coefficient can also be expressed with the mean diffusion jump distance of ${}^3$He atom in the glass $\langle \Delta r \rangle$ as:

$$D = \frac{\langle \Delta r \rangle^2}{6\tau} \tag{4.2}$$

where $\tau$ is the mean time between diffusion jumps

$$\tau = \tau_0 e^{E_{dif}/kT} \tag{4.3}$$

where $\tau_0 = \langle \Delta r \rangle^2 / 6 D_0$.

Let $n_g$ be the number of atoms dissolved in the surface layer of mean thickness $\langle \Delta r \rangle$, the rate at which ${}^3$He atoms enter and leave the surface layer of the glass is

then $n_g/6\tau$. $n_g$ should be proportional to the solubility $S$ of $^3$He in the glass, so for a spherical cell

$$n_g = \frac{6NkT\langle \Delta r \rangle S}{d} \tag{4.4}$$

where d is the diameter of the cell, N is the total number of free $^3$He atoms.

The intrinsic relaxation time $T_i$ is longer than $\tau$, the time it takes for $^3$He to leave the $\langle \Delta r \rangle$ layer, for most trapping sites in the glass. However, $T_i$ for a paramagnetic site is shorter than $\tau$, thus will completely relax the nuclear spin of a $^3$He atom. The relaxation time of $^3$He in permeable glass cells is controlled by absorption of the atoms in the surface layer at paramagnetic sites. The average nuclear relaxation time of a $^3$He trapped in the glass close to a $Fe^{3+}$ ion (one common type of paramagnetic impurity in glass) is [?]:

$$\frac{1}{T_i} \approx \frac{3}{5}\frac{\mu_{He}^2\mu_B^2 g^2}{\hbar^2 b^6}\frac{T_{Fe}}{1+\omega_0^2 T_{Fe}^2} \tag{4.5}$$

where $\mu_{He}$ is the nuclear dipole moment of $^3$He, $\mu_B$ is the Bohr magneton, g is the g factor of the $Fe^{3+}$ $(^6S_{5/2})$ ion, and b is the distance between the spins. Taking b as 1 $\mathring{A}$ and g as 5.9 [?], $T_i$ is $\sim 10^{-11}$ s, which is 10 times smaller than the shortest $\tau$.

Even a small amount of paramagnetic impurities among the trapping sites in the glass can provide dominating contribution on the $^3$He spin relaxation. Assuming during the random walk of $^3$He atom in the glass, there are on average $\beta$ atoms in its vicinity, and atom fraction of paramagnetic impurities is $N_{impurity}$, the relaxation time due to absorption is if $T_i \ll \tau$:

$$T_{ab} = \frac{6N\tau}{\beta N_{Fe}n_g} \tag{4.6}$$

For impermeable glasses such as GE180, the relaxation rate due to absorption into the glass walls is typically negligible. The dominating relaxation mechanism here is

adsorption of $^3$He on the glass wall in vicinity of a paramagnetic site.

The sticking time $tau_s$ is given by Frenkel's Law:

$$\tau_s = \tau_{s0} e^{E_{ad}/kT} \tag{4.7}$$

where $\tau_{s0}$ is on the order of $10^{-13}$ s for most solid surfaces [?], $E_{ad}$ is the adsorption energy. At room temperature, we have $\tau_s \sim \tau_{s0} \sim 10^{-13}$ s. The number of atoms hitting the wall per unit time and unit area is given by $\frac{1}{4}n\bar{v}$, where n is the number density of $^3$He gas and $\bar{v}$ is the mean velocity. For a spherical cell with diameter d, the number of atoms adsorbed on the wall is

$$n'_g = \frac{3N\bar{v}\tau_s}{2d} \tag{4.8}$$

The intrinsic relaxation time $T'_i$ of a $^3He$ near a paramagnetic site on the wall is much longer than the sticking time $\tau_s$. The average number of collisions required to depolarize $^3$He is $T'_i/\tau_s$, thus the relaxation time due to adsorption is

$$T_{ad} = \frac{NT'_i}{N_{impurity}n'_g} \tag{4.9}$$

The total relaxation rate is the sum of that due to adsorption and absorption (for permeable glasses):

$$\frac{1}{T_{wall}} = \frac{1}{T_{ad}} + \frac{1}{T_{ab}} \tag{4.10}$$

Substitute Eq. ??, ?? into Eq. ?? and Eq. ??, ?? into Eq. ??, the wall relaxation rate can be written as

$$\begin{aligned}
\frac{1}{T_{wall}} = &\frac{\beta N_{impurity}kT\langle\Delta r\rangle S}{d\tau_0}e^{-E_{dif}/kT} \\
&+ \frac{3N_{impurity}\bar{v}\tau_{s0}}{2dT'_i}e^{E_{ad}/kT}
\end{aligned} \tag{4.11}$$

84

Fitzsimmons *et al.* [**?**] found by using impermeable aluminosilicate glass, the relaxation due to absorption can be greatly reduced thus increasing the total relaxation time. Heil *et al.* reported [**?**] glass cells that were internally coated with metallic films provided even longer relaxation time. Ce was one of the metals that greatly reduced wall relaxation rate as it blocks $^3$He atoms from diffusing into the glass walls and it also has a low adsorption energy which leads to very short sticking time. For SEOP (Spin-Exchange Optical Pumping), we automatically profit from the Rb film which covers the inner surface of the pumping chamber. Similarly, another way to eliminate relaxation due to absorption is to coat the inner surface with sol-gel [**?**]. It is a mixture of aluminum nitrate nonahydrate $Al(NO_3)_39H_2O$, ethanol and deionized water. The sol-gel coating also improves relaxation time by blocking $^3$He atoms from diffusing into the glass.

### 4.2.2 Relaxation on Metal Surfaces

# Bibliography

[1] High-performance nuclear-polarized $^3$He targets for electron scattering based on spin-exchange optical pumping. *PhD thesis, University of Virginia*, 2010.

[2] E. Babcock, I. A. Nelson, S. Kadlecek, and T. G. Walker. $^3$He polarization-dependent epr frequency shifts of alkali-metal˘$^3$He pairs. *Phys. Rev. A*, 71:013414, Jan 2005.

[3] F. Bloch. Nuclear induction. *Phys. Rev.*, 70:460–474, Oct 1946.

[4] G. D. Cates, S. R. Schaefer, and W. Happer. Relaxation of spins due to field inhomogeneities in gaseous samples at low magnetic fields and low pressures. *Phys. Rev. A*, 37:2877–2885, Apr 1988.

[5] G. D. Cates, D. J. White, T.-R. Chien, S. R. Schaefer, and W. Happer. Spin relaxation in gases due to inhomogeneous static and oscillating magnetic fields. *Phys. Rev. A*, 38:5092–5106, Nov 1988.

[6] E. M. M. V. Romalis and G. D. Cates. Pressure broadening of rb $d_1$ and $d_2$ lines by $^3$he, $^4$he, $n_2$, and xe: line cores and near wings. *Phys. Rev. A*, 56(6), 1997.

[7] I. I. Rabi, N. F. Ramsey, and J. Schwinger. Use of rotating coordinates in magnetic resonance problems. *Rev. Mod. Phys.*, 26:167–171, Apr 1954.

[8] M. L. R.Barbe and F. Laloe. Experimental verifications - measurement of the he3 self-diffusion coefficient. 35:935–951, 1974.

[9] M. V. Romalis and G. D. Cates. Accurate $^3$He polarimetry using the rb zeeman frequency shift due to the Rb$-^3$He spin-exchange collisions. *Phys. Rev. A*, 58:3004–3011, Oct 1998.

[10] W. H. Thad G. Walker. Spin-exchange optical pumping of noble-gas nuclei. *RMP Colloquia.*

# Appendix A

# Appendix title

This is Appendix A.

You can have additional appendices too (*e.g.*, `apdxb.tex`, `apdxc.tex`, *etc.*). If you don't need any appendices, delete the appendix related lines from `thesis.tex` and the file names from `Makefile`.